

Bulk Convergence of Cloud-Resolving Simulations of Moist Convection over Complex Terrain

WOLFGANG LANGHANS,* JUERG SCHMIDLI, AND CHRISTOPH SCHÄR

Institute for Atmospheric and Climate Science, ETH Zurich, Zurich, Switzerland

(Manuscript received 24 September 2011, in final form 30 January 2012)

ABSTRACT

The explicit treatment of moist convection in cloud-resolving models with kilometer-scale horizontal resolution is increasingly used for atmospheric research and numerical weather prediction purposes. However, several previous studies have implicitly questioned the physical validity of this approach, as the accurate representation of the structure and evolution of moist convective phenomena requires considerably higher resolution. Unlike these studies, which focused on single convective systems, here the convergence of bulk properties of an ensemble of moist convective cells in kilometer-scale simulations is considered.

To address the convergence, the authors focus on the bulk net heating and moistening in a large control volume, the associated vertical fluxes, and the diurnal evolution of regionally averaged precipitation. Besides numerical convergence, “physical” convergence (Reynolds number increases with resolution) is addressed for two conceptually different subgrid-mixing approaches (1D mesoscale and 3D LES). Simulations are conducted for a 9-day period of diurnal summer convection over the Alps, using a large computational domain with grid spacings of 4.4, 2.2, 1.1, and 0.55 km and grid-independent topography.

Results show that for the model and episode considered, the simulated bulk properties and vertical fluxes converge numerically toward the 0.55-km solution. In terms of bulk effects, differences between the simulations are surprisingly small, even within the physical convergence framework that exhibits a sensitivity of the small-scale dynamics and ensuing convective structures to the horizontal resolution. Despite some sensitivities related to the applied turbulence closure, the results support the feasibility of kilometer-scale models to appropriately represent the bulk feedbacks between moist convection and the larger-scale flow.

1. Introduction

Operational weather prediction centers are increasingly applying numerical simulations on grids with horizontal mesh spacings on the order of 1 km and advances to similar resolutions are expected for regional-scale climate projections in the near future. At kilometer-scale grid spacings deep convection is explicitly simulated on the grid and the need for parameterizations

of subgrid-scale processes is reduced. The general experience from both short-range numerical weather prediction (NWP) (Richard et al. 2007; Lean et al. 2008; Schwartz et al. 2009; Weusthoff et al. 2010) and longer-range projections (Grell et al. 2000; Hohenegger et al. 2008a) is that such convection-permitting simulations outperform convection-parameterizing simulations, since the fundamental nonhydrostatic processes of deep convective thunderstorms are explicitly resolved (Klemp and Wilhelmson 1978; Weisman et al. 1997).

Still, the characteristic scales of such storms are approximately of the size of the grid spacing or even smaller (Craig and Dörnbrack 2008). Owing to this issue, an uncertainty is tied to the horizontal grid spacing and subgrid mixing in these models. Several studies have addressed the requirements for subgrid turbulence closures

* Additional affiliation: Centre for Climate Systems Modeling (C2SM), Zurich, Switzerland.

Corresponding author address: Wolfgang Langhans, Institute for Atmospheric and Climate Science, Universitätstrasse 16, 8092 Zurich, Switzerland.
E-mail: wolfgang.langhans@env.ethz.ch

in kilometer-scale simulations. Bryan et al. (2003) argued that, for deep organized convection, convergence of large-eddy simulations (LES) due to Reynolds-number similarity is not yet obtained at grid spacings $O(100\text{ m})$. As outlined by Wyngaard (2004), in a strict sense neither LES nor 1D closures used in mesoscale models are applicable to kilometer-scale simulations of deep convection.

The effective resolution in convection-permitting simulations is found to be still limited by the horizontal grid spacing rather than by the typically much smaller vertical level spacing (Skamarock 2004). Several authors have reported simulation deficits linked to insufficiently dense horizontal grids. For example, Petch et al. (2002) argued that a horizontal grid spacing of $\Delta x = 800\text{ m}$ results in a delay of the formation of both shallow and deep convection compared to a $\Delta x = 125\text{ m}$ simulation. Recent attempts to achieve better convergence properties of convective features have included higher-order closures (Cheng and Xu 2006), the allowance of backscatter (Weinbrecht and Mason 2008), and the development of mixed schemes (Moeng et al. 2010).

The focus of the aforementioned studies is on *physical convergence* (usually simply referred to as convergence)—that is, the insensitivity of flow statistics with respect to *both* grid spacing and the physics of the flow. Alternatively, one may address *numerical convergence*, and consider an increasingly resolved numerical representation of a fixed set of governing equations. In the former case, finer grid resolutions typically result in smaller eddy viscosities and hence larger Reynolds numbers (when using appropriate subgrid-scale turbulence parameterizations). In contrast, numerical convergence describes the limiting behavior of a discretization scheme to reach the solution to a fixed continuous problem at infinitely small grid spacing (and time step). According to the Lax–Richtmyer theorem, a scheme is numerically convergent if it is stable, provided the initial value problem is well posed and the numerical scheme is consistent (Lax and Richtmyer 1956; Rosinger 1980). A fixed continuous problem is not provided if grid-dependent parameterizations for eddy viscosities are used.

To motivate this study and further discriminate between numerical and physical convergence, we illustrate numerical convergence properties from simulations of a two-dimensional, dry, linear flow over a bell-shaped mountain. The details of the setup are explained in the appendix. While a reference run ($\Delta x = 0.5\text{ km}$) fully resolves the atmospheric response to the orographic forcing, a $\Delta x = 4\text{ km}$ simulation, having only a couple of grid points across the mountain, deviates from the reference solution (see the appendix). Figure 1 illustrates

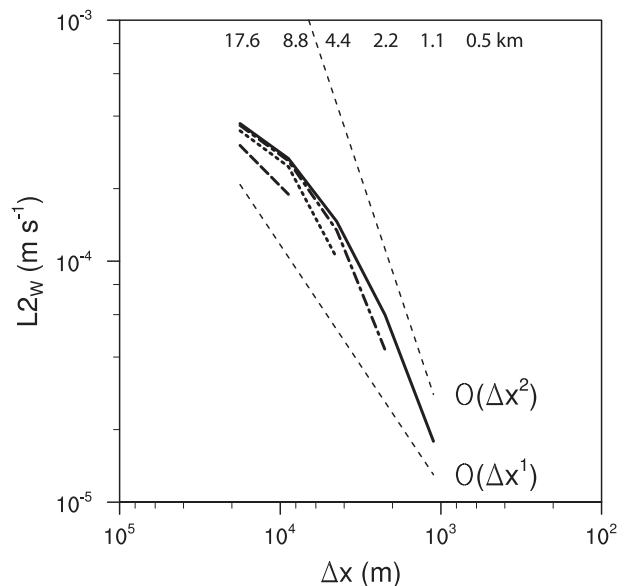


FIG. 1. The L2 norm (i.e., rms error) for linear hydrostatic flow over a 2D bell-shaped hill (height 1 m, half-width 10 km) computed for vertical velocity and with respect to a $\Delta x = 550\text{ m}$ simulation (solid) and to lower-resolution simulations (dashed curves). Thin dashed lines correspond to first- and second-order convergence. The setup of these simulations is further described in the appendix.

numerical convergence for the model used in our study toward the high-resolution reference solution. As demonstrated in Fig. 1, the solution converges—at a very similar order—toward coarser reference simulations ($\Delta x > 0.5\text{ km}$). Apparently, the order of numerical convergence can be estimated even from poorly resolved reference runs (e.g., $\Delta x = 4\text{ km}$). We will later use this result when assessing numerical convergence for simulations of deep convection.

Numerical convergence has been analyzed for LES of shear-driven and buoyancy-driven turbulent flows by Mason and Callen (1986) and Mason and Brown (1999), respectively, using simulations with a constant turbulent length scale, such that the grid independence of the turbulence parameterization is enforced. A similar approach with grid-independent physics has also been applied to global-scale simulations (Boer and Denis 1997).

In the context of convection-permitting simulations it is, however, of uttermost relevance to better resolve the dynamics of the flow on finer numerical meshes (e.g., higher Reynolds number flows). Thereby, the costs of finer resolution can pay off in a reduced need for complex turbulence parameterizations. Thus, as also discussed by, for example, Mason (1994) and Cullen and Brown (2009), a small resolution sensitivity of the flow statistics, such as the total (resolved plus

unresolved) variances, that even further decreases with higher resolution is crucial in the framework of physical convergence.

Previous studies of physical convergence have considered the structure and evolution of moist convective flows in idealized settings. Specifically they addressed squall lines (Bryan et al. 2003), moist thermals (Craig and Dörnbrack 2008), or supercell developments (Fiori et al. 2010). All of these studies found that substantially higher resolution than used in kilometer-scale modeling was required to appropriately resolve the underlying characteristic spatial structures and/or temporal evolutions of the phenomena considered. However, while the focus on the statistics of single thermals or cloud system is relevant, it is not a priori evident whether it is the appropriate convergence test for real-case cloud-resolving simulations. At these small scales, perturbation-doubling times are often very short (a few hours) and deterministic predictability may be lost early in the simulations (Hohenegger et al. 2008b). The goal of kilometer-scale simulations is thus not primarily to resolve individual moist convective elements (which are anyway not predictable), but rather to represent the overall statistics of an ensemble of convective elements (e.g., the statistical distribution of cells and precipitation intensity) as well as the associated interactions with the larger-scale flow. The latter point is particularly germane in so-called superparameterizations in global climate models (e.g., Khairoutdinov and Randall 2001; Grabowski 2001) that willingly adopt a modeling framework with unphysical small-scale structures in order to improve the bulk fluxes. More recently, the convergence of bulk flow statistics in idealized simulations of maritime tropical convection has been addressed by Khairoutdinov et al. (2009).

In contrast to previous studies, we thus focus on the convergence of regional-scale properties of real-case kilometer-scale simulations of deep convection in terms of bulk heat and moisture budgets. Thereby, we investigate both numerical and physical convergence properties. In analogy to the LES study presented by Mason and Brown (1999), numerical convergence is addressed by using constant turbulent length scales in the subgrid-scale mixing parameterization. To cover the uncertainty tied to turbulence closures at the kilometer scales (see Wyngaard 2004), physical convergence is analyzed using resolution-dependent turbulent length scales within a 1D PBL closure and a LES closure.

The computational framework is based on real-case simulations covering a large computational domain [$O(1000 \text{ km})$] covering the European Alps over extended-range time scales [$O(1 \text{ week})$]. The period considered is characterized by a persistent fair-weather

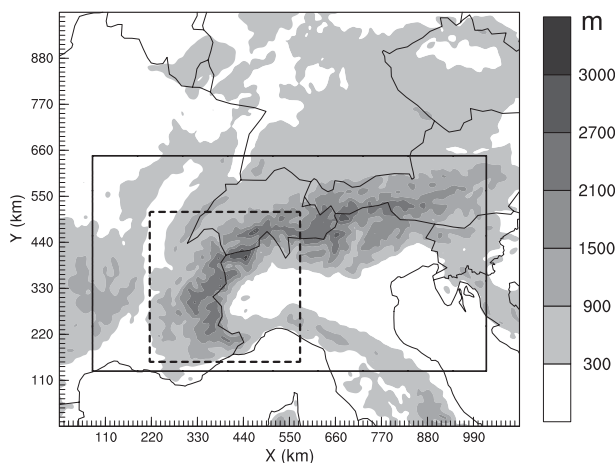


FIG. 2. Topography (m) of the COSMO model domain. The black solid box indicates the position of the control volume and horizontal distance is given in kilometers. The dashed box shows the subdomain for which cloud liquid water is shown in Fig. 6.

flat-pressure summer situation with locally triggered orographic convection and a pronounced diurnal cycle. This type of convection occurs frequently during summertime, is generally only weakly organized, contributes significantly to the atmospheric heating and moistening over the Alpine region, and yields pronounced interactions with the meso- β -scale flow (Lugauer and Winkler 2005).

We introduce the analyzed bulk metrics in section 2 and describe the numerical model in section 3. Basic simulation characteristics are shown in section 4a and results on numerical convergence and physical convergence of bulk properties are presented in sections 4b and 4c, respectively. We discuss our findings in section 5 and conclude with section 6.

2. Heat and moisture budget formulation

To study the convergence of bulk flow properties, heat and moisture budgets for a large Alpine control volume covering an area of $970 \times 515 \text{ km}^2$ are investigated (see Fig. 2). Its top is located right above the highest mountain peaks at 4 km MSL. Although the planetary boundary layer (PBL) height varies in space and time, the fluxes through the top might be seen as a crude estimate for the exchange between the PBL and the free atmosphere. The formulation and derivation of the integrated budget equations is described in this section.

a. Bulk heat budget

Following Schmidli and Rotunno (2010) we integrate the density-weighted thermodynamic equation over a volume V and normalize it by the total volume mass. The resulting atmospheric heat budget can then be written as

$$\underbrace{\frac{1}{M} \int_V \rho \frac{\partial \theta}{\partial t} dV}_{\text{NET}} = \underbrace{-\frac{1}{M} \int_V \rho \mathbf{v} \cdot \nabla \theta dV}_{\text{ADV}} + \underbrace{\frac{1}{M} \int_V -\frac{1}{c_p} (\mathbf{V} \cdot \mathbf{R}) dV}_{\text{RAD}} + \underbrace{\frac{1}{M} \int_V -\frac{1}{c_p} (\mathbf{V} \cdot \mathbf{H}) dV}_{\text{TURB}} + \underbrace{\frac{1}{M} \int_V \rho L_{v,f} dV}_{\text{MIC}}, \quad (1)$$

with the net heat storage tendency NET, advection ADV of potential temperature θ , radiative and sensible heat flux convergence RAD and TURB, respectively, latent heating MIC, density ρ , sensible heat flux $\mathbf{H} = c_p \rho \overline{\mathbf{v}'' \theta''}$, heat capacity at constant pressure c_p , radiative energy flux \mathbf{R} , latent heating rate $L_{v,f}$ and total volume mass M . Units are kelvins per second for each term. Double primes appearing in \mathbf{H} indicate subgrid-scale fluctuations.

Alternatively, ADV can be converted into flux form using the anelastic approximation. To this end, the potential temperature is decomposed into a volume-averaged density-weighted temperature and its deviation; that is,

$$\theta = \theta_0 + \tilde{\theta} \quad \text{with} \quad \theta_0 = \frac{1}{M} \int_V \rho \theta dV. \quad (2)$$

Assuming anelasticity, this can be expressed as

$$\text{ADV} = -\frac{1}{M} \int_V \nabla \cdot (\tilde{\theta} \rho \mathbf{v}) dV. \quad (3)$$

Then applying Gauss' theorem yields a transport equation, given as

$$\begin{aligned} \text{ADV} + \text{TURB} = & -\frac{1}{M} \int_A \rho \tilde{\theta} w dA - \frac{1}{c_p M} \int_A H_{\text{top}} dA \\ & + \frac{1}{c_p M} \int_A H_{\text{sfc}} dA - \frac{1}{M} \int_S \rho \tilde{\theta} v_{\text{hn}} dS, \end{aligned} \quad (4)$$

with A denoting the surface (top) area of the box, S the area of its four sidewalls, v_{hn} the horizontal velocity component normal to the sidewalls (positive for outward directed flow), and H_{sfc} and H_{top} the subgrid turbulent heat flux at the ground and the top, respectively. The four terms on the rhs relate to resolved (first term) and subgrid-scale (second term) vertical heat exchange through the top, to a subgrid-scale flux at the surface (third term), and to resolved horizontal flux through the sidewalls (fourth term). The latter will be abbreviated as θ_{hn} . The subgrid-scale lateral fluxes into the volume are

much smaller than the resolved fluxes and thus not shown in this paper.

b. Bulk water vapor budget

Similar to the heat equation the water vapor budget can be written in volume-integrated density-weighted form as

$$\begin{aligned} \underbrace{\frac{1}{M} \int_V \rho \frac{\partial q_v}{\partial t} dV}_{Q_{\text{NET}}} = & \underbrace{-\frac{1}{M} \int_V \rho \mathbf{v} \cdot \nabla q_v dV}_{Q_{\text{ADV}}} \\ & + \underbrace{\frac{1}{M} \int_V -\frac{1}{l_v} (\mathbf{V} \cdot \mathbf{L}) dV}_{Q_{\text{TURB}}} \\ & + \underbrace{\frac{1}{M} \int_V \rho S_{v,f} dV}_{Q_{\text{MIC}}} \end{aligned} \quad (5)$$

with water vapor storage tendency Q_{NET} , water vapor advection Q_{ADV} , latent heat flux convergence Q_{TURB} , and microphysical water vapor source/sink Q_{MIC} . The latent heat flux is given as $\mathbf{L} = l_v \rho \overline{\mathbf{v}'' q_v''}$ with the latent heat of vaporization l_v ; $S_{v,f}$ are microphysical source/sink rates, such as evaporation of rain or depositional growth of snow.

c. Ensemble-averaged budget for a 9-day simulation period

Since convection shares many characteristics with a stochastically random process in space and time, an analysis of convergence should be based on the ensemble mean of the volume-integrated tendencies or bulk fluxes. We therefore consider a 9-day simulation period (0000 UTC 11 July–0600 UTC 20 July 2006) characterized by quasiperiodically reoccurring diurnal convection over the Alps, regard each single day as one realization of moist convection, and compute ensemble-mean quantities by averaging over all nine days. This procedure is supported by the presence of a dominating quasiperiodic forcing provided by surface shortwave radiation, while the ambient atmospheric conditions are rather constant with little inflow through the lateral domain boundaries. Note, however, that the convective development on a specific day might depend on the conditions emanating from the preceding day(s).

The same simulation period has been documented and investigated in several previous studies (MeteoSchweiz 2006; Hohenegger et al. 2008a; Schlemmer et al. 2011; Langhans et al. 2012b). Intensive summertime convection occurs during each afternoon over the Alps. The synoptic situation is characterized by a large-scale ridge over central

Europe. Over the Alps the associated flat pressure distribution leads to intensive summertime convection during each afternoon.

Any resolved variable a at location x, y, z and at phase Φ (i.e., time of day) on day n can then be decomposed as

$$a(x, y, z, \Phi; n) = \langle a \rangle(z, \Phi; n) + a'(x, y, z, \Phi; n) \quad (6)$$

into a horizontally averaged part (first term; $\langle \dots \rangle$ denotes horizontal average) and a resolved deviation from this spatial average (second term). The normalized bulk flux $M^{-1}\langle \tilde{\theta}(\rho w) \rangle(x, y, z, \Phi; n)$ [see Eq. (4)] can then be decomposed into a bulk mean flux and a grid-scale (resolved) turbulent flux, written at height z and phase Φ as

$$\frac{1}{M}\langle \tilde{\theta}(\rho w) \rangle(z, \Phi) = \frac{1}{M}\langle \tilde{\theta} \rangle \langle \rho w \rangle + \frac{1}{M}\langle \tilde{\theta}'(\rho w)' \rangle, \quad (7)$$

with overbars denoting the ensemble (i.e., phase) average for the 9-day period. Substitution of this flux at $z = 4$ km into the ensemble-averaged form of Eq. (4) yields

$$\begin{aligned} \text{ADV} + \text{TURB} = & - \underbrace{A \frac{1}{M}\langle \tilde{\theta} \rangle \langle \rho w \rangle}_{A_M} - \underbrace{A \frac{1}{M}\langle \tilde{\theta}'(\rho w)' \rangle}_{A_{\text{GS}}} \\ & - \underbrace{\frac{A}{c_p} \frac{1}{M}\langle H_{\text{top}} \rangle}_{T_{\text{top}}} + \underbrace{\frac{A}{c_p} \frac{1}{M}\langle H_{\text{sfc}} \rangle}_{T_{\text{sfc}}} + \theta_{\text{hflx}}, \end{aligned} \quad (8)$$

where A_M and A_{GS} denote resolved advective terms, and T_{top} and T_{sfc} subgrid turbulent terms. Equivalently, a transport equation can be derived for water vapor, as

$$Q\text{ADV} + Q\text{TURB} = - \underbrace{A \frac{1}{M}\langle \tilde{q}_v \rangle \langle \rho w \rangle}_{QA_M} - \underbrace{A \frac{1}{M}\langle \tilde{q}_v'(\rho w)' \rangle}_{QA_{\text{GS}}} - \underbrace{\frac{A}{l_v} \frac{1}{M}\langle L_{\text{top}} \rangle}_{QT_{\text{top}}} + \underbrace{\frac{A}{l_v} \frac{1}{M}\langle L_{\text{sfc}} \rangle}_{QT_{\text{sfc}}} + Q_{\text{hflx}}. \quad (9)$$

The ensemble-averaged transport results from a bulk mean flux A_M , bulk grid-scale (resolved) turbulent flux A_{GS} , and bulk unresolved turbulent flux T_{top} through the top of the volume and a bulk turbulent surface flux T_{sfc} . The last terms (θ_{hflx} and Q_{hflx}) are ensemble-averaged horizontal fluxes into the volume. All of these terms, the tendencies due to the total fluxes through the top $\theta_{\text{vflx}} = A_M + A_{\text{GS}} + T_{\text{top}}$ and $Q_{\text{vflx}} = QA_M + QA_{\text{GS}} + QT_{\text{top}}$, and the ensemble-averages of the full budget equations (1) and (5) will be analyzed in this paper. All heat and moisture tendencies from Eqs. (1) and (5) correspond exactly to those computed within the code and are extracted online as described by Langhans et al. (2012a). Note that A_{GS} and QA_{GS} are not limited to the grid scale, but could potentially also include contributions from the meso- β scale.

3. Model configuration

a. General description

The budget terms introduced in section 2 are obtained from simulations using the nonhydrostatic Consortium for Small-Scale Modeling (COSMO) model, which solves the fully compressible governing equations (Steppeler et al. 2003; Doms and Förstner 2004). The continuous equations are discretized in time using a split-explicit third-order Runge–Kutta scheme (Klemp and Wilhelmson

1978; Wicker and Skamarock 2002) and a fifth-order upstream-biased advection scheme is used in horizontal space. Vertical advection is computed implicitly using a centered second-order scheme. For advection of moisture scalars a positive-definite scheme (Bott 1989) is applied. Further details on the convection-permitting version of COSMO are presented by Baldauf et al. (2011).

The modeling domain covers $1100 \times 990 \text{ km}^2$, a large region centered over the European Alps (see Fig. 2). In the vertical 46 terrain-following model levels are employed with the lowest mass level at ~ 33 m AGL and a horizontal model top at 20 hPa. Simulations with horizontal grid spacings of 4.4, 2.2, 1.1, and 0.55 km are conducted. All simulations resolve the nonhydrostatic dynamics of deep convection without parameterization (Weisman et al. 1997) and the high-resolution limit is given by computational constraints. The grid configurations correspond to a total number of 3, 10, 42, and 166 million grid points, respectively. The long time steps used are 30, 15, 8, and 4 s, respectively. The European Centre for Medium-Range Weather Forecasts provides initial and 6-hourly boundary conditions for the period of investigation, which has been described in section 2c. Initial soil moisture is obtained from a long-term simulation (see Jäger et al. 2008) using the climate version COSMO-CLM.

The diabatic and subgrid-scale part of the model comprises radiative transfer (Ritter and Geleyn 1992),

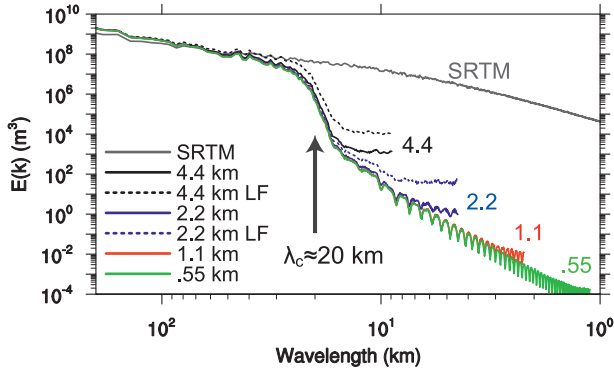


FIG. 3. Spectral energy density distributions computed from the topography of the four different numerical truncations. Domain averages have been computed from 1D spectra and the raw data (SRTM) at full resolution is included for comparison. Spectra of reduced low-pass filtered (LF) topography are shown as well.

land surface processes (Heise et al. 2003), and single-moment cloud microphysics (Reinhardt and Seifert 2006). Two different parameterizations for subgrid-scale turbulent transport are applied, as described below. Note that a similar model setup has been applied in Langhans et al. (2012b). However, the current setup differs in several aspects: Horizontal diffusion is exclusively computed as a subgrid mixing term, more stringent numerical limiting of explicit vertical TKE diffusion is applied, and grid-scale cloud cover is determined using an empirical relation to the relative humidity.

b. Topography

A unique property of all conducted simulations is the treatment of the topography on the different numerical grids. The topographic resolution is kept constant in wavenumber space in order to avoid more detailed valley structures on finer resolved grids. Thus, the effect of the grid spacing on convection can be isolated from the effects due to modified topographic forcing. Nearly identical spectral representations of the topography are obtained by applying the Raymond (1988) fifth-order low-pass filter to the 4.4-km topography and interpolating successively to the next higher resolution. The same procedure is applied to soil properties. The resulting topographic spectrum reveals a constant energy cutoff wavelength of ~ 20 km (Fig. 3). Beyond the cutoff all spectra contain at least two orders of magnitude less variance than the very high resolution data provided by the Shuttle Radar Topography Mission (SRTM). Preliminary tests using modified small-scale filtering (see spectra LF in Fig. 3) demonstrated that the remaining energy contained beyond the cutoff does not affect our results.

c. Turbulent diffusion

The method chosen here is to consider a 1D PBL closure typically used in mesoscale applications and a 3D closure commonly used in LES of convective storms. Each model exhibits deficiencies at kilometer scales and has not originally been designed for such scales (see Bryan et al. 2003; Wyngaard 2004). The motivation is to touch upon the uncertainties stemming from the formulation of unresolved turbulent processes and its influence on the convergence of bulk Alpine-scale properties. Both approaches try to describe unresolved turbulent fluxes by applying the eddy-viscosity assumption and the gradient-diffusion hypothesis (“K theory”).

1) 1D TKE-BASED MODEL

The eddy viscosity is related to turbulent kinetic energy (TKE), diagnosed as described by Raschendorfer (2001). This TKE formulation is based on the original description of a “closure on level 2.5” by Mellor and Yamada (1982) developed to represent turbulent mixing in mesoscale atmospheric models using the homogeneous planetary boundary layer assumption (HPBL) (e.g., Stull 1988). Thereby, the eddy viscosities for heat $K_{H,M}^v$ and momentum K_M^v are parameterized as

$$K_{H,M}^v = l_v S_{H,M} \sqrt{2\text{TKE}}, \quad (10)$$

with the turbulent length scale l_v formulated following Blackadar (1962) as

$$l_v = l_\infty \frac{\kappa z}{\kappa z + l_\infty}. \quad (11)$$

A constant asymptotic turbulent length scale of $l_\infty = 100$ m is used for all numerical resolutions; $S_{H,M}$ are stability functions for heat and momentum, respectively, and κ is the von Kármán constant.

Following Smagorinsky (1963), the eddy viscosity for second-order lateral diffusion can be related to the horizontal grid-scale rate of strain as

$$K_M^h = [c_s (\Delta x \Delta y)^{1/2}]^2 [(D_{11} - D_{22})^2 + 4D_{12}^2]^{1/2}, \quad (12)$$

with $D_{ij} = (1/2)(\partial u_i / \partial x_j + \partial u_j / \partial x_i)$. The viscosity for scalar mixing is given as K_M^h / Pr with the turbulent Prandtl number $\text{Pr} = 1/3$. As suggested by Takemi and Rotunno (2003), we increase the Smagorinsky constant from its original value of ~ 0.2 to $c_s = 0.25$ to account for finite difference errors. The turbulent length scale for horizontal mixing $l_h = c_s \times (\Delta x \Delta y)^{1/2}$ is usually linearly related to the mesh width.

As indicated by Mason and Sykes (1982) the horizontal velocity fluxes near the surface are underestimated by the horizontal velocity gradients and are even larger than the vertical fluxes. Thus, similar to the Mason and Sykes approach, we apply an anisotropic viscosity K^h if $K^h > K^v$ but retain an isotropic viscosity $K^h = K^v$ otherwise. Note that this model is not completely three-dimensional as vertical diffusion due to $\langle w''u'' \rangle$ and $\langle w''v'' \rangle$, respectively, is still neglected in the corresponding momentum equations. This is an assumption commonly applied in the framework of the HPBL.

2) SMAGORINSKY–LILLY MODEL

LESs have been designed to simulate the energy transfer from resolved to unresolved scales across an inertial subrange of locally isotropic three-dimensional turbulence. Although in principle not fully justified (Pope 2000; Bryan et al. 2003), such turbulence models have commonly been used for kilometer-scale studies of moist convection within the cloud-modeling community (Klemp and Wilhelmson 1978; Petch et al. 2002; Takemi and Rotunno 2003). Compared to a 1D mesoscale approach, all variances of turbulent fluctuations appearing in the Reynolds-averaged momentum equations are considered. The Smagorinsky (1963) original proposal has been extended by Lilly (1962) to include the effects of buoyancy, such that the eddy viscosity is given as

$$K_M^{h,v} = l_s^2 D \sqrt{1 - \frac{\text{Ri}}{\text{Pr}}} \quad (13)$$

with the characteristic rate of strain $D = (2D_{ij} D_{ij})^{1/2}$, Smagorinsky length scale $l_s = c_s(\Delta x \Delta y \Delta z)^{1/3}$ (see also Fig. 4), and (deformation) Richardson number

$$\text{Ri} = \begin{cases} N_m^2/D^2 & \text{for saturated air} \\ N^2/D^2 & \text{for unsaturated air.} \end{cases} \quad (14)$$

The moist static stability N_m is computed following Durran and Klemp (1982b) and N is related to the gradient of the virtual potential temperature. Again, c_s is taken to be 0.25.

d. Overview of simulations

Three sets of simulations using different turbulent closures will be presented in this paper. An overview of the applied turbulent length scales is presented in Fig. 4 and a summary of the characteristics of the three simulation sets is given in Table 1. Simulation NC_1D addresses numerical convergence and thus applies a grid-independent parameterization of turbulent mixing. The 1D TKE-based closure is used in combination with

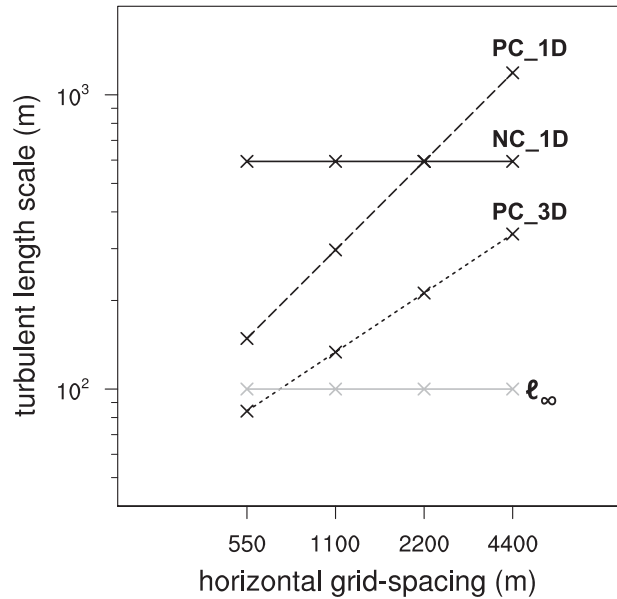


FIG. 4. Turbulent length scales for horizontal diffusion for NC_1D (solid), PC_1D (long dashed), and PC_3D (short dashed) as a function of horizontal grid spacing. The Smagorinsky length scale l_s (used in PC_3D) is computed here for $\Delta z = 100$ m and the gray line indicates the asymptotic turbulent length scale l_∞ used for vertical diffusion in NC_1D and PC_1D.

the 2D Smagorinsky closure for lateral diffusion, but the turbulent length scale for horizontal mixing is kept constant at $l_h = c_s \times 2200$ m. Note that the asymptotic length scale l_∞ for vertical mixing is also grid independent such that the eddy viscosities are independent of the horizontal grid spacing in NC_1D.

Physical convergence is studied with two further sets with prefix ‘‘PC’’. PC_1D uses the same setup as NC_1D but uses a grid-dependent length scale for horizontal mixing (as described in section 3c). In PC_3D the Smagorinsky–Lilly 3D LES closure is used. Therein, both horizontal and vertical mixing are proportional to l_s such that the eddy viscosities decrease with smaller grid spacings and Reynolds numbers increase.

TABLE 1. Overview of three simulation sets and specific turbulent length scales applied for horizontal l_h and vertical mixing l_v . The homogeneous planetary boundary layer assumption (HPBL) is applied in the ‘‘mesoscale’’ 1D TKE-based PBL closure.

	Set		
	NC_1D	PC_1D	PC_3D
Turbulence closure	1D TKE	1D TKE	Smagorinsky–Lilly
HPBL	Yes	Yes	No
l_h	$c_s \times 2200$ m = const	$c_s \times (\Delta x \Delta y)^{1/2}$	$c_s \times (\Delta x \Delta y \Delta z)^{1/3}$
l_v	Eq. (11)	Eq. (11)	$c_s \times (\Delta x \Delta y \Delta z)^{1/3}$

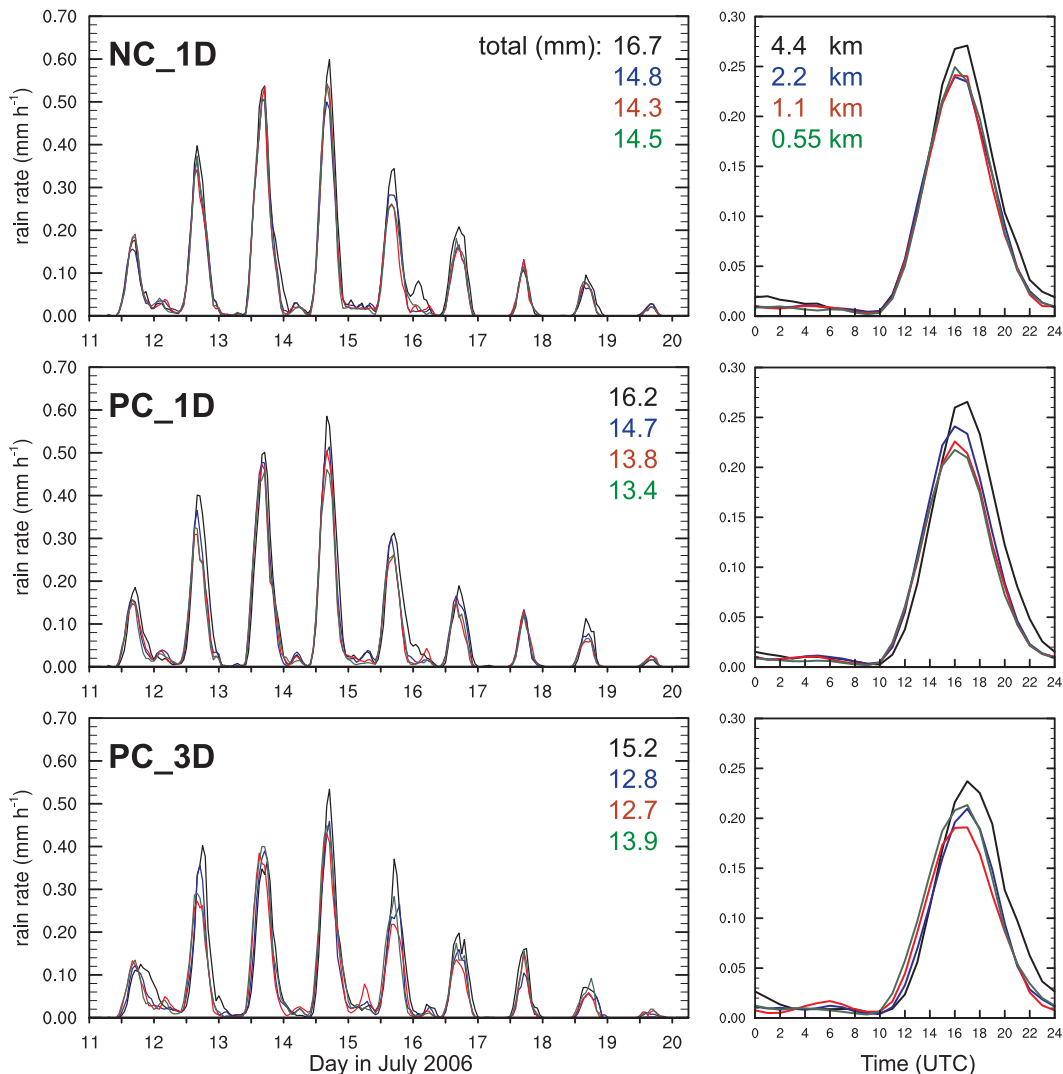


FIG. 5. (left) Time series and (right) mean diurnal cycles of surface precipitation in the alpine subdomain (see Fig. 2) from NC_1D, PC_1D, and PC_3D and for the different grid spacings: 4.4 (black), 2.2 (blue), 1.1 (red), and 0.55 km (green). Total precipitation (mm) of each simulation is indicated within the panels.

4. Results

We divide this section into three parts. Before the convergence of bulk alpine-scale properties will be presented in detail, some general characteristics of the simulations are described. Then, results on numerical convergence of the Alpine heat and water vapor budget and of bulk vertical fluxes are presented for the simulation set NC_1D. Finally, physical convergence properties obtained from simulations PC_1D and PC_3D are presented.

a. Basic simulation characteristics

Figure 5 shows time series and mean diurnal cycles of area-averaged surface precipitation obtained from the

three simulation sets. All simulations generate precipitation peaking in the late afternoon for each of the nine days. Convection appears to be particularly strong during the first five days and less pronounced during the last four days. The quasiperiodicity of convective precipitation exhibits the physics of the thermally triggered development of diurnal convection over topography.

Although the diurnal precipitation peak seems to decrease with smaller grid spacings on several of the simulated days for all three sets, the differences related to the grid spacing are small for grid spacings less than 4 km. The 4-km runs produce more precipitation than runs using smaller grid spacings on most of the days. This is reflected also in more pronounced diurnal peak rates

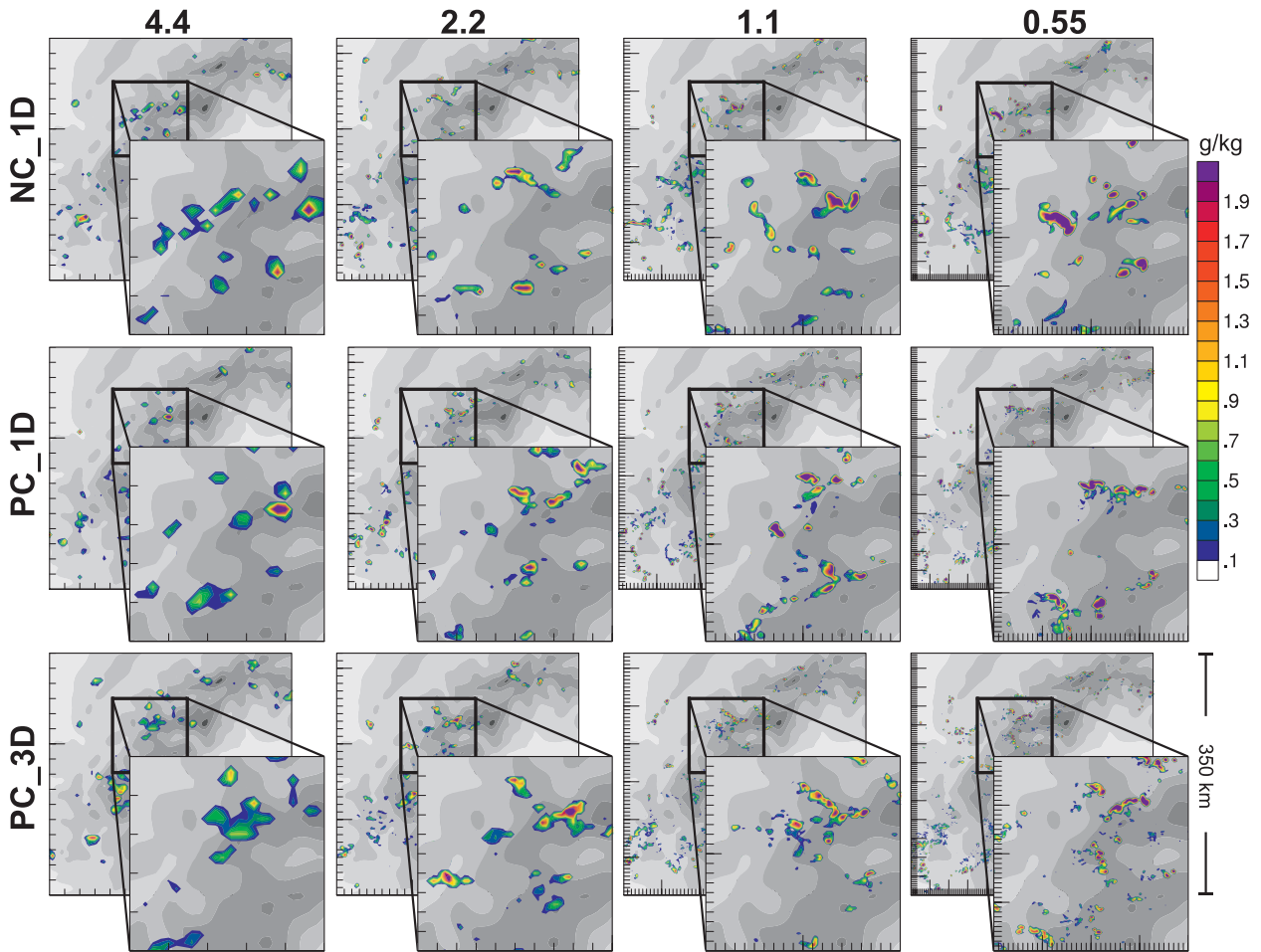


FIG. 6. Display of cloud liquid water distributions at 6 km MSL, 1400 UTC 14 July, as simulated by the different setups in a subdomain located over the southwestern parts of the Alpine arc (see Fig. 2). Small (large) tick marks correspond to a distance of $5\Delta x$ ($50\Delta x$).

of the corresponding mean diurnal cycles and in larger precipitation totals (see Fig. 5).

While the timing of precipitation in NC_1D is unaffected by the grid spacing, precipitation is generated slightly earlier in PC_1D and PC_3D at higher resolution. This is related to the effects of eddy viscosity on the convective growth. As demonstrated by Fuhrer and Schär (2005), the fastest-growing unstable modes are shifted to larger wavenumbers with smaller eddy viscosities such that small-scale perturbations grow more rapidly. Similar results were obtained from the Petch et al. (2002) idealized convection-permitting simulations that showed earlier and less intensive precipitation maxima with decreasing grid spacings.

Figure 6 shows snapshots of cloud liquid water distributions at 1400 UTC 14 July at 6 km MSL for a southwestern subsection of the domain (see Fig. 2), where mature orographic convection has formed. NC_1D reveals similar cloud size distributions for all grid spacings.

In contrast, smaller and more numerous cloud features are simulated with smaller grid spacings in PC_1D and PC_3D due to smaller eddy viscosities (higher Reynolds numbers). Thus, the energy-containing scales are shifted to ever smaller scales as the grid spacing is decreased in PC_1D and PC_3D. This is in line with Bryan et al. (2003), who did not find convergence of cloud system properties for $\Delta x \geq 125$ m. Interestingly, the impact of grid spacing on the amount and timing of the area-averaged precipitation is nevertheless small (Fig. 5).

b. Numerical convergence

1) VOLUME-INTEGRATED TENDENCIES

As mentioned in section 2c we are interested in the ensemble-averaged (i.e., phase-averaged) tendencies in this paper, shown in Fig. 7 for NC_1D. Apparently, the control volume's net tendencies are surprisingly insensitive to a refinement in grid spacing (see Figs. 7a,c).

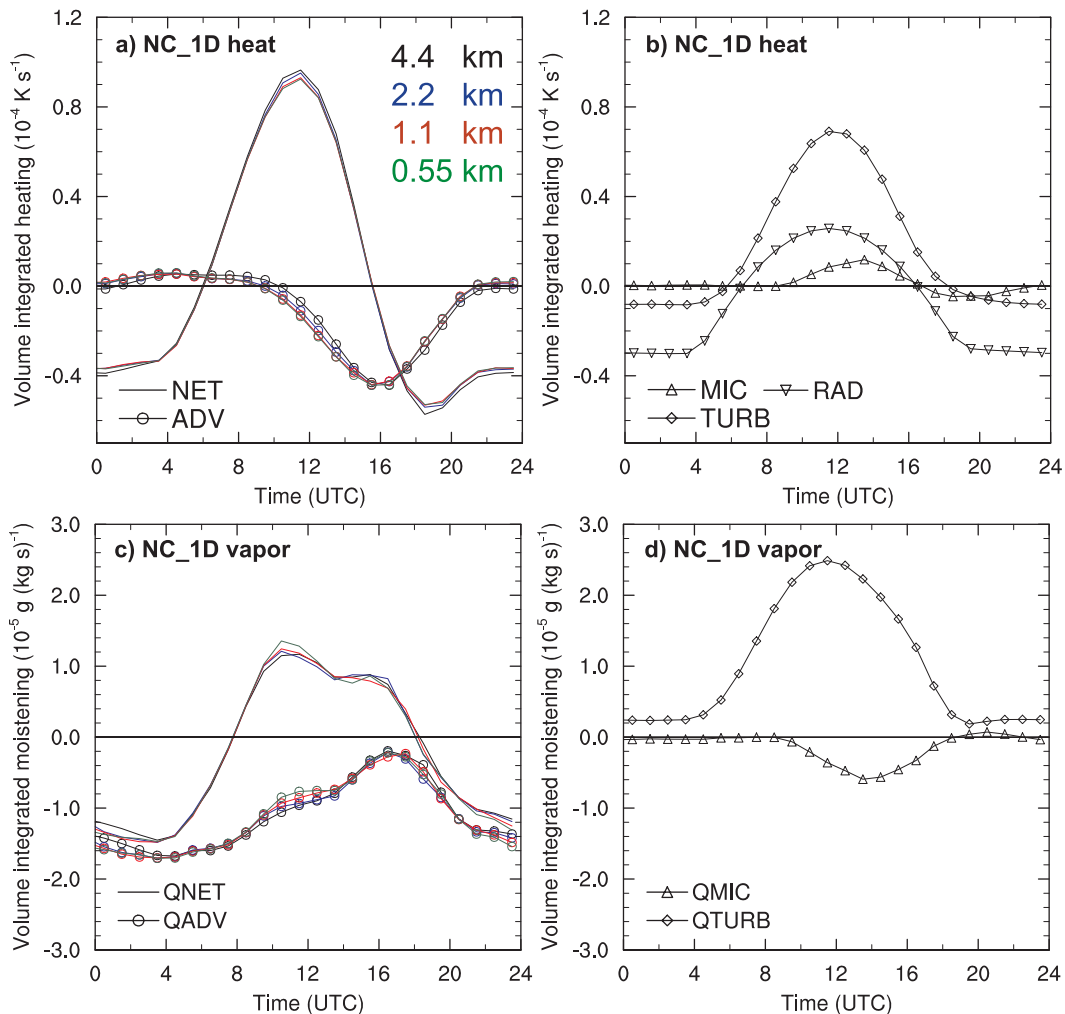


FIG. 7. Mean diurnal cycles of volume-integrated (a),(b) heating rates (10^{-4} K s^{-1}) and (c),(d) moistening rates ($10^{-5} \text{ g kg}^{-1} \text{ s}^{-1}$) from NC_1D using (black) 4.4-km, (blue) 2.2-km, (red) 1.1-km, and (green) 0.55-km grid spacing, respectively; (a) and (c) show net tendencies and advective tendencies and (b) and (d) indicate the rhs terms in Eqs. (1) and (5), respectively. Since TURB, $QTURB$, MIC, $QMIC$, and RAD are almost grid independent, only the 4.4-km run is shown for each variable.

Only very small differences in net heating and net moistening are produced around midday. All simulations warm the control volume during the period between 0600 and 1600 UTC and cool the volume otherwise (Fig. 7a). Moistening occurs between 0800 and 1800 UTC (Fig. 7c).

The impact of resolution on the net advection of heat ADV and water vapor $QADV$ is also small (see Figs. 7a,c). The advective tendencies of a scalar can be interpreted as fluxes through the volume's boundaries [see Eq. (3)]. Figure 7a shows that during the afternoon the imported air is colder than the exported air. The water vapor content is reduced by advection throughout the day (see Fig. 7c).

The diabatic contributions to the budgets are hardly affected by the grid spacing and thus only shown for the

4-km run (see Figs. 7b,d). The net tendencies are mostly driven by turbulent flux convergence during daytime. Together with the radiative flux convergence quasiperiodic diabatic heating is provided. Between 1000 and 1800 UTC, condensation depletes vapor and releases latent heat.

2) PBL TO FREE ATMOSPHERE EXCHANGE

The vertical transport is analyzed by evaluating the corresponding terms in the transport equations (8) and (9). The decomposition of the total flux through the box's top presented in Figs. 8b and 8d reveals entrainment of heat and detrainment of vapor by the subgrid fluxes T_{top} and QT_{top} , respectively. These fluxes are rather small compared to T_{sfc} and QT_{sfc} (not shown).

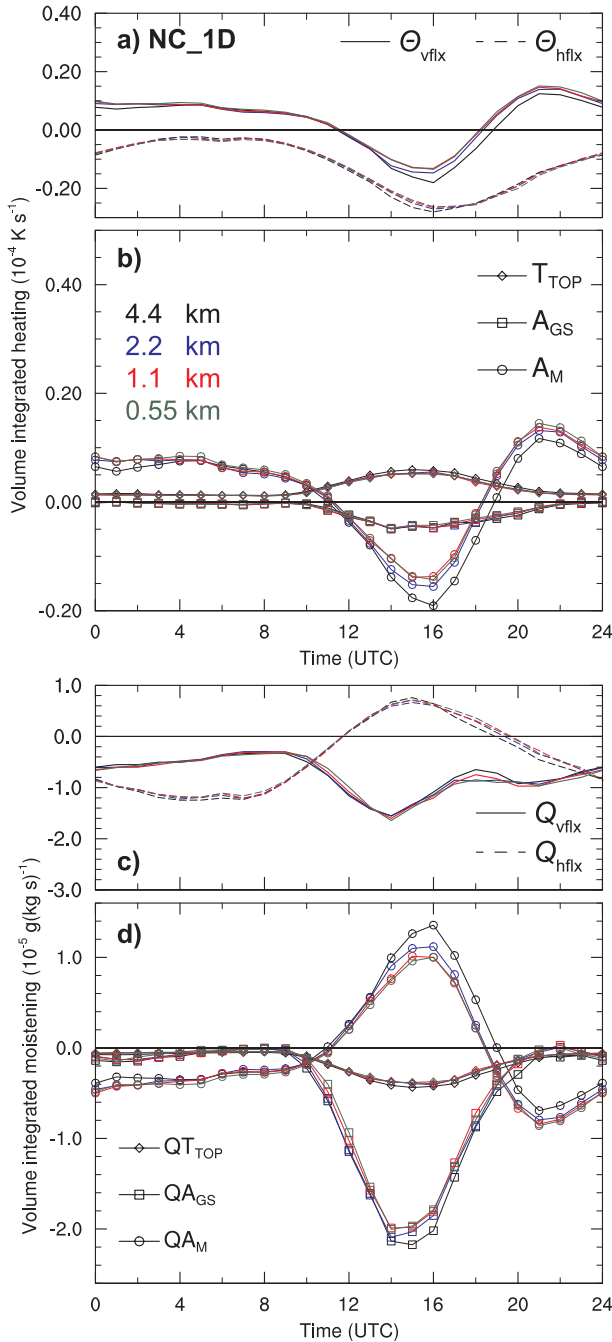


FIG. 8. Mean diurnal cycles of (a),(b) heat and (c),(d) moisture tendencies due to fluxes through the volume’s top at 4 km MSL and through its lateral boundaries from NC_1D. Shown are the total vertical and horizontal fluxes in (a) and (c) and the decomposed fluxes from Eqs. (8) and (9) in (b) and (d), respectively, for 4.4-km (black), 2.2-km (blue), 1.1-km (red), and 0.55-km (green) grid spacings.

The resolved vertical fluxes of heat, A_M and A_{GS} , export heat during the afternoon. While the grid-scale flux QA_{GS} also exports moisture, the mean flux QA_M increases the volume’s vapor content, as it transports

relatively dry air through the volume’s top upward. The upward directed fluxes A_{GS} and QA_{GS} indicate that the resolved turbulent fluxes are dominated by warm and moist rising thermals.

The total upward transport of heat through the box’s top θ_{vflx} decreases only marginally with higher resolution, since the bulk mean export of heat A_M decreases slightly (Figs. 8a,b). The total vertical water vapor transport Q_{vflx} is also hardly modified (Fig. 8c), since both bulk import of dry air QA_M and resolved export of moist air QA_{GS} decrease slightly with higher resolution (Fig. 8d). Numerical convergence will be quantified further below.

Interestingly, also the lateral fluxes θ_{hflx} and Q_{hflx} through the volume’s sides (Figs. 8a,c) are independent of the grid spacing. The horizontal fluxes contribute substantially to the net advective tendencies (ADV and QADV in Figs. 7b,d) and are found to cool and moisten the control volume during daytime. Thus, the lateral fluxes add to the loss of heat by vertical export (Fig. 8a) and counteract the water vapor loss through the volume’s top (Fig. 8c) during the afternoon. This is in agreement with Lugauer and Winkler (2005) and Weissmann et al. (2005), who showed that a thermally driven plain–mountain circulation typically extends to the adjacent Alpine forelands.

3) DEEP CONVECTIVE FLUXES

As described above, both the volume-integrated heating/moistening and the bulk vertical transport through the volume’s top are relatively insensitive to the horizontal grid spacing for set NC_1D. Here, we complete our analysis by studying the bulk fluxes at higher elevations, which are mainly related to deep convective fluxes (DCF) during daytime. The DCF of heat and vapor is calculated as the total vertical flux:

$$DCF_{\theta} = \langle w \rangle \langle \dot{\theta} \rangle + \langle w' \theta' \rangle + \left\langle \frac{1}{c_p \rho} H_v \right\rangle, \quad (15)$$

which is the sum of a bulk mean flux $\langle w \rangle \langle \dot{\theta} \rangle$, a bulk resolved mesoscale flux $\langle w' \theta' \rangle$, and a bulk unresolved vertical turbulent flux $\langle w'' \theta'' \rangle = \langle (c_p \rho)^{-1} H_v \rangle$ in kinematic units. The bulk fluxes are evaluated for a plane located at 6 km MSL above the control volume and $\dot{\theta}$ (\dot{q}_v in case of DCF_{q_v}) is defined as the deviation from the average temperature of this larger (i.e., deeper) volume.

Figure 9 shows the ensemble-averaged total flux of heat (DCF_{θ}) and of water vapor (DCF_{q_v}). At this altitude an upward (downward) directed heat flux cools (warms) the subjacent volume during the day (night). The upward transport of moisture dries the volume throughout the day. The spread among the simulations

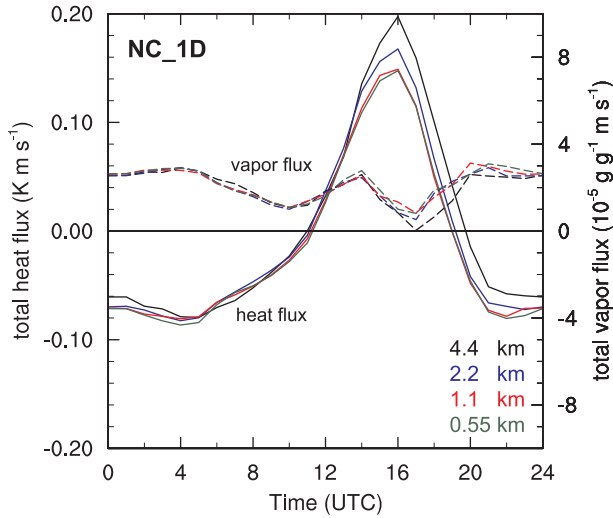


FIG. 9. Mean diurnal cycles of total bulk deep-convective heat flux DCF_{θ} (solid) and moisture flux DCF_{qv} (dashed) through a horizontal plane at 6 km MSL. Both fluxes are given in kinematic units for 4.4-km (black), 2.2-km (blue), 1.1-km (red), and 0.55-km (green) grid spacing from NC_1D.

is small and appears to become smaller with resolution, indicating numerical convergence.

4) NUMERICAL CONVERGENCE OF BULK PROPERTIES

In analogy to the convergence study conducted for an idealized flow over a hill (see Fig. 1), we aim at simple metrics that indicate whether real kilometer-scale simulations of diurnal moist convection converge or not. To this end, error norms with respect to the $\Delta x = 0.55$ km simulation are computed for the bulk flow properties presented above. According to results presented in Fig. 1, the $\Delta x = 0.55$ km run may serve as a reference for a convergence test, although it might not fully resolve the convective flow considered. However, as apparent also from the idealized flow (see Fig. 1), the estimated order of convergence might depend upon the numerical resolution.

Since we are primarily interested in the 9-day averaged behavior an error norm for the averaged bulk quantities is computed. The RMSE $_{\Psi}$ error norm for an ensemble-averaged parameter Ψ simulated with grid spacing Δx is here computed with respect to the $\Delta x = 550$ m simulation, as

$$RMSE_{\Psi} = \left\{ \frac{1}{N} \sum_{n=1}^N [\Psi_{\Delta x}(n) - \Psi_{550}(n)]^2 \right\}^{1/2} \quad (16)$$

with $N = 24$ for hourly data. In analogy to the presentation of numerical convergence of an idealized flow

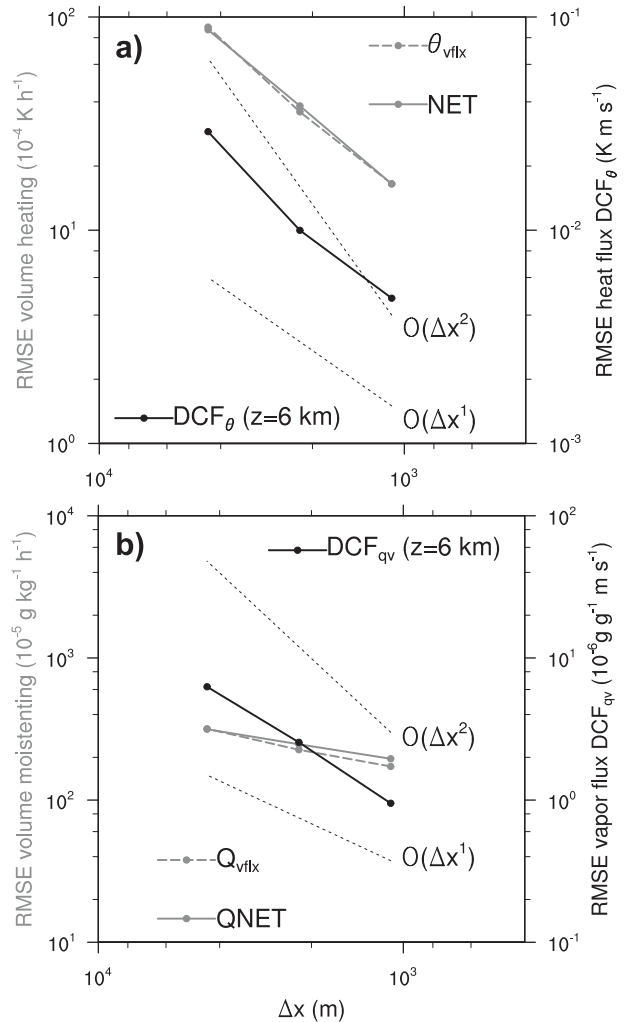


FIG. 10. RMSE norm computed from NC_1D with respect to the 550-m solution for ensemble-averaged quantities (a) NET, θ_{vflx} , and DCF_{θ} and (b) QNET, Q_{vflx} , and DCF_{qv} . The thin dashed lines indicate first- and second-order convergence.

(see Fig. 1), Fig. 10 shows the RMSE for averaged bulk quantities in a log-log diagram. For all quantities the decrease of RMSE with smaller grid spacings confirms the convergent behavior of the kilometer-scale simulations, although the convergence is slow for QNET and Q_{vflx} .

To summarize, numerical convergence is obtained for several bulk diagnostics related to the Alpine scale.

c. Physical convergence

1) VOLUME-INTEGRATED TENDENCIES

The volume-integrated heat and moisture tendencies of simulations PC_1D and PC_3D are shown in Figs. 11 and 12. The simulations yield very similar diurnal cycles of the net heating and moistening rates (Figs. 11a,c).

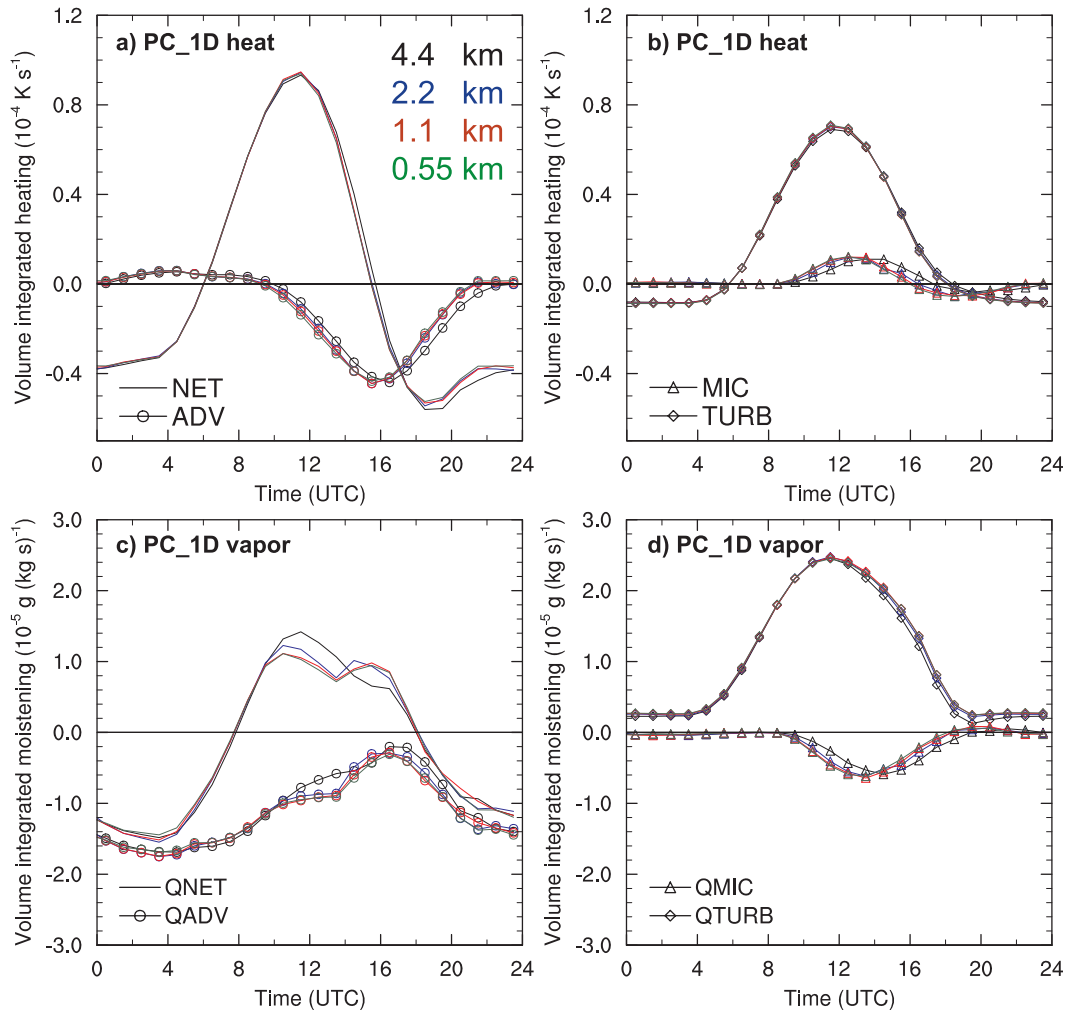


FIG. 11. Mean diurnal cycles of volume-integrated (a),(b) heating rates (10^{-4} K s^{-1}) and (c),(d) moistening rates ($10^{-5} \text{ g kg}^{-1} \text{ s}^{-1}$) from PC_1D. Lines with markers (see legend) indicate the rhs terms in Eqs. (1) and (5).

Compared to NC_1D, the sensitivity of the daytime net moistening to horizontal resolution is only slightly increased in PC_1D and PC_3D.

Considerable compensation is found among diabatic tendencies. While the turbulent and microphysical tendencies in PC_1D are almost independent of the grid spacing (Figs. 11b,d), both turbulent and microphysical tendencies in PC_3D reveal a significant dependence on the grid spacing (Figs. 12b,d). Since the Smagorinsky length scale l_s used for vertical turbulent mixing decreases with smaller grid spacings in PC_3D, entrainment of heat and detrainment of moisture is decreased. Thus, the control volume remains cooler and more humid and consequentially condensation is increased. Both the latent heat release and the condensational vapor sink are increased (Figs. 12b,d) and compensate the reduced tendencies from subgrid-scale mixing. Owing to this compensation the net heating and moistening

in the control volume reveal little sensitivity to the grid resolution.

2) PBL TO FREE ATMOSPHERE EXCHANGE

Bulk tendencies related to the vertical transport through the top of the control volume at 4 km MSL are shown in Fig. 13 for both PC_1D and PC_3D. In PC_1D the total bulk flux of heat and moisture (Figs. 13a,c) is basically unaffected by the grid spacing. Only the 4-km run deviates from the higher-resolution runs, as its heat and moisture export is delayed compared to the higher-resolution runs. The resolved turbulent fluxes A_{GS} and QA_{GS} increase only slightly with higher resolution around midday (Figs. 13b,d). This increase was not observed in NC_1D and is linked to better-resolved convective motions. The weakly modified behavior of the bulk resolved turbulent fluxes is also reflected in the bulk fluxes A_M and QA_M .

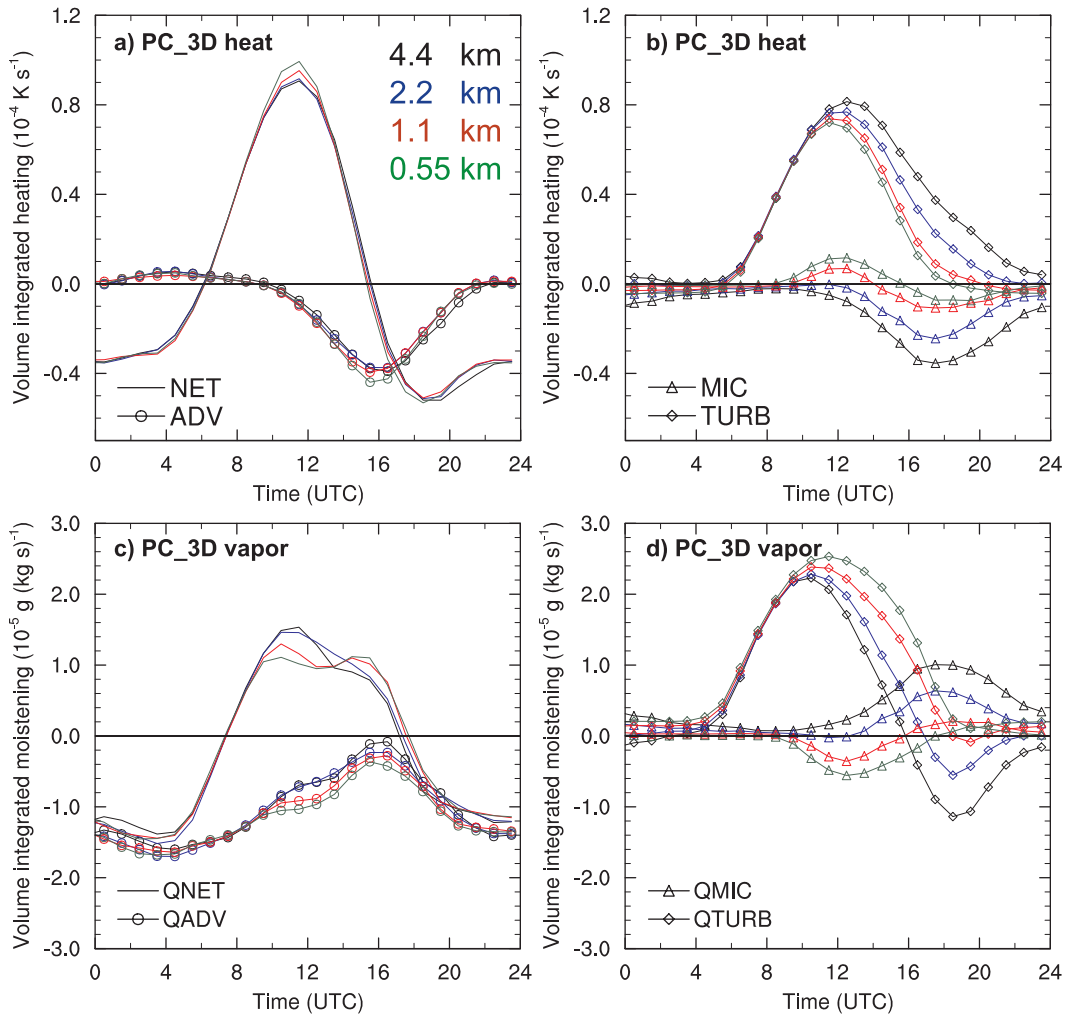


FIG. 12. As in Fig. 11, but for PC_3D.

In contrast to PC_1D, the total vertical transport of heat and moisture is considerably altered with resolution in PC_3D (see Figs. 13e,g), since the subgrid-scale fluxes T_{top} and QT_{top} (Figs. 13f,h) depend on the grid spacing. As already mentioned, both the heat entrainment and the water vapor detrainment decrease with smaller grid spacings due to the grid dependency of the turbulent length scale. The increase of the resolved turbulent heat and moisture fluxes A_{GS} and QA_{GS} (Figs. 13f,h) is even more pronounced around midday than in PC_1D; in particular, higher-resolution runs result in a larger moisture export by QA_{GS} around midday. Still, in PC_3D the total exchange through the volume's top is dominated by the strongly modified subgrid fluxes, which result in stronger cooling and moistening with higher resolution (Figs. 13e,g). As with NC_1D, both PC_1D and PC_3D yield mostly grid-independent lateral fluxes into the volume (Figs. 13a,c,e,g).

In short, the sensitivity of the bulk vertical fluxes to horizontal resolution is found to be small in PC_1D, but large in PC_3D. Thus, physical convergence seems unlikely for the vertical fluxes in PC_3D. This will be quantified in section 4c(4).

3) DEEP CONVECTIVE FLUXES

Deep convective fluxes at 6 km MSL [see Eq. (15)] from PC_1D and PC_3D are shown in Fig. 14. Similar to the resolved vertical transport at 4 km MSL (see Fig. 13) a slight shift to earlier times can be recognized for DCF_{θ} and DCF_{qv} with higher resolution around midday. The obtained spread among the fluxes is considerably smaller for PC_1D than for PC_3D. Nevertheless, the spread among simulations with different grid spacings appears to decrease with higher resolution for PC_3D. Analysis of the subgrid-scale fluxes $\langle w''\theta'' \rangle$ and $\langle w''q_v'' \rangle$ (not shown) revealed that, in analogy to the transport at

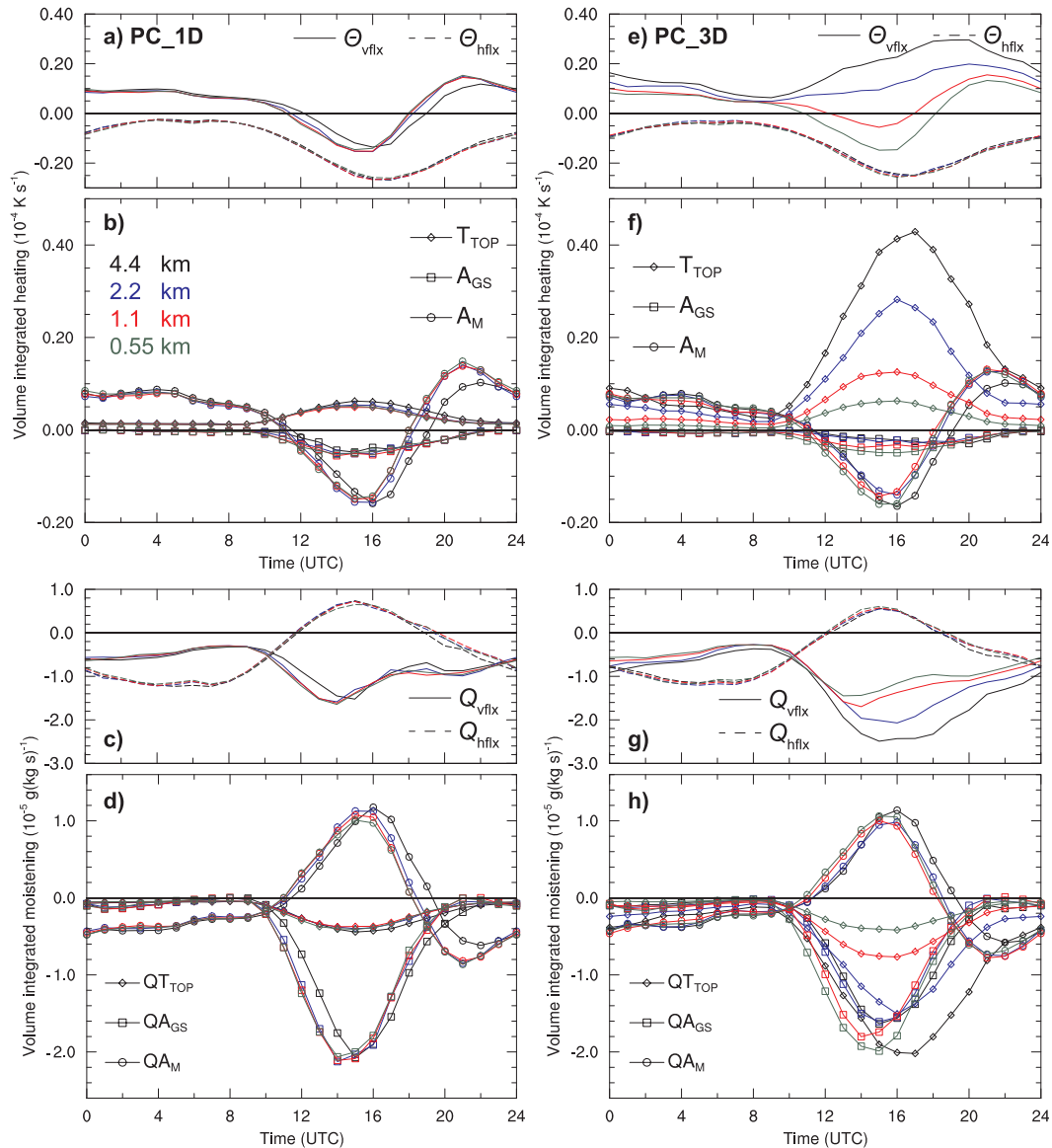


FIG. 13. As in Fig. 8, but for (a)–(d) PC_1D and (e)–(h) PC_3D.

4 km MSL, the grid dependency of the total fluxes is tied to the LES closure.

To better understand the scales involved in the convective transport of heat and moisture we computed spectra of vertical velocity (Figs. 15a,c,e) and cospectra for heat and moisture flux (Figs. 15b,d,f) at 6 km MSL and averaged over the 9-day period at 1600 UTC. The results obtained from the heat flux analysis point at the same behavior as the moisture flux analysis and are thus not shown. Since turbulent length scales are forced to be grid independent in NC_1D, the simulated energetic scales are independent of numerical resolution (Figs. 15a,b). In contrast, the energetic scales are shifted to smaller scales in PC_1D and PC_3D (Figs. 15c,e)

indicating that convective motions are—as also described by Bryan et al. (2003)—not yet converged at kilometer scales. As a consequence, additional contributions to the moisture flux are resolved with higher numerical resolution (Figs. 15d,f). Interestingly, the total flux integrated over all scales is barely affected by the numerical resolution since the flux contribution carried by larger scales decreases with higher resolution.

4) PHYSICAL CONVERGENCE OF BULK PROPERTIES

The sensitivity of flow statistics to the grid spacing is expected to become smaller with increasing resolution

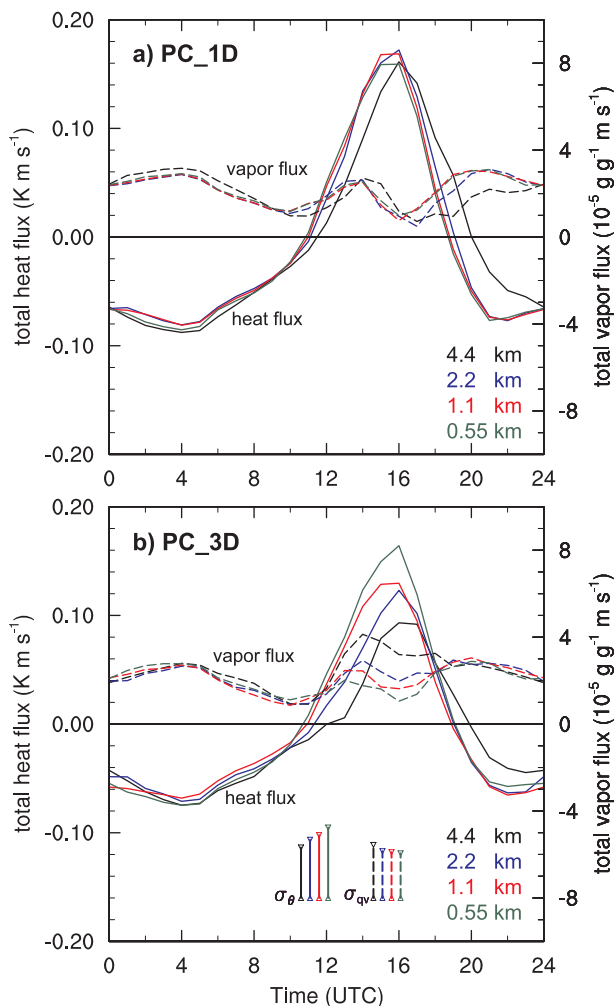


FIG. 14. As in Fig. 9, but for (a) PC_1D and (b) PC_3D. Characteristic values of DCF (σ) that are used for the computation of NRI [Eq. (17)] are given as an example for PC_3D in (b).

in physically converging simulations. To study this, a rather simple metric is considered that illustrates the resolution dependence of the mean diurnal cycle of each bulk property. This parameter should measure the simulated absolute error of a bulk property with respect to the simulation with the next smaller grid spacing. Moreover, the metric should relate the spread between two grid spacings to a characteristic value of the considered bulk property in order to allow statements about the relative magnitude of the spread.

A normalized resolution increment (NRI) of an ensemble-averaged bulk property $\Psi(\Phi)$ simulated with a grid spacing Δx is computed as the rms difference with respect to the simulation using $\Delta x/2$ normalized by a characteristic value σ . Defining σ as an average absolute

value of $\Psi(\Phi)$ from the 550-m simulation, NRI is given as

$$\text{NRI} = \frac{\text{RMSE}_{\Delta x}}{\sigma_{550}} = \frac{\sqrt{\frac{1}{N} \sum_{\Phi=1}^N [\Psi_{\Delta x}(\Phi) - \Psi_{\Delta x/2}(\Phi)]^2}}{\frac{1}{N} \sum_{\Phi=1}^N |\Psi_{550}(\Phi)|} \quad (17)$$

with $N = 24$ for hourly data. As an example, σ is shown for DCF in Fig. 14b.

Figures 16a and 16b show the normalized increments NRI of the mean diurnal cycle of volume-integrated heat and moisture tendencies. NRI is evaluated here for both the net tendencies and the tendencies due to the total bulk vertical transport through the top of the volume. Owing to the compensating behavior found for PC_3D, the resulting NRI of NET and QNET is typically around 10% or even smaller for both PC_1D and PC_3D. While NRI of θ_{vflx} and Q_{vflx} decreases from around 30% at 4.4 km below 10% at 1.1-km grid spacing in PC_1D, significantly larger differences are found for PC_3D. The heat flux θ_{vflx} in PC_3D is highly grid dependent for all three grid spacings, such that the normalized increment is $\sim 90\%$ at 4.4 km, $\sim 95\%$ at 2.2 km, and still $\sim 60\%$ at 1.1 km. The resolution increment of the moisture flux Q_{vflx} decreases $\sim 40\%$ at 4.4 km, $\sim 36\%$ at 2.2 km, and to $\sim 16\%$ at 1.1 km for PC_3D.

NRI has also been computed for DCF at 6 km MSL and for surface precipitation (Figs. 16c,d). Apparently, for both PC_1D and PC_3D the increments between simulations decrease with higher resolution, indicating physical convergence of deep convective fluxes and precipitation. An exception is found for NRI of DCF_{qv} simulated by PC_3D, which is slightly larger at 1.1 km than at 2.2 km. The NRI is around 10% or even smaller for the 1.1-km run of PC_1D. The strong influence of the horizontal grid spacing on the subgrid part of the vertical fluxes in PC_3D is reflected also in the total fluxes. The 2.2- and 1.1-km runs of PC_3D yield larger NRIs for DCF as the corresponding runs of PC_1D.

Our findings on the physical convergence at kilometer scales can be briefly summarized as follows. The influence of horizontal resolution on the net heating and moistening of the control volume is small for both turbulence parameterizations. A monotonic decrease of the resolution sensitivity is found for all considered bulk quantities in PC_1D. A more complicated behavior is found for PC_3D since the total vertical transport at 4 and 6 km MSL is strongly affected by the horizontal resolution. Thus, a decreasing sensitivity to resolution, that is, physical convergence, is not necessarily obtained for all bulk properties in PC_3D.

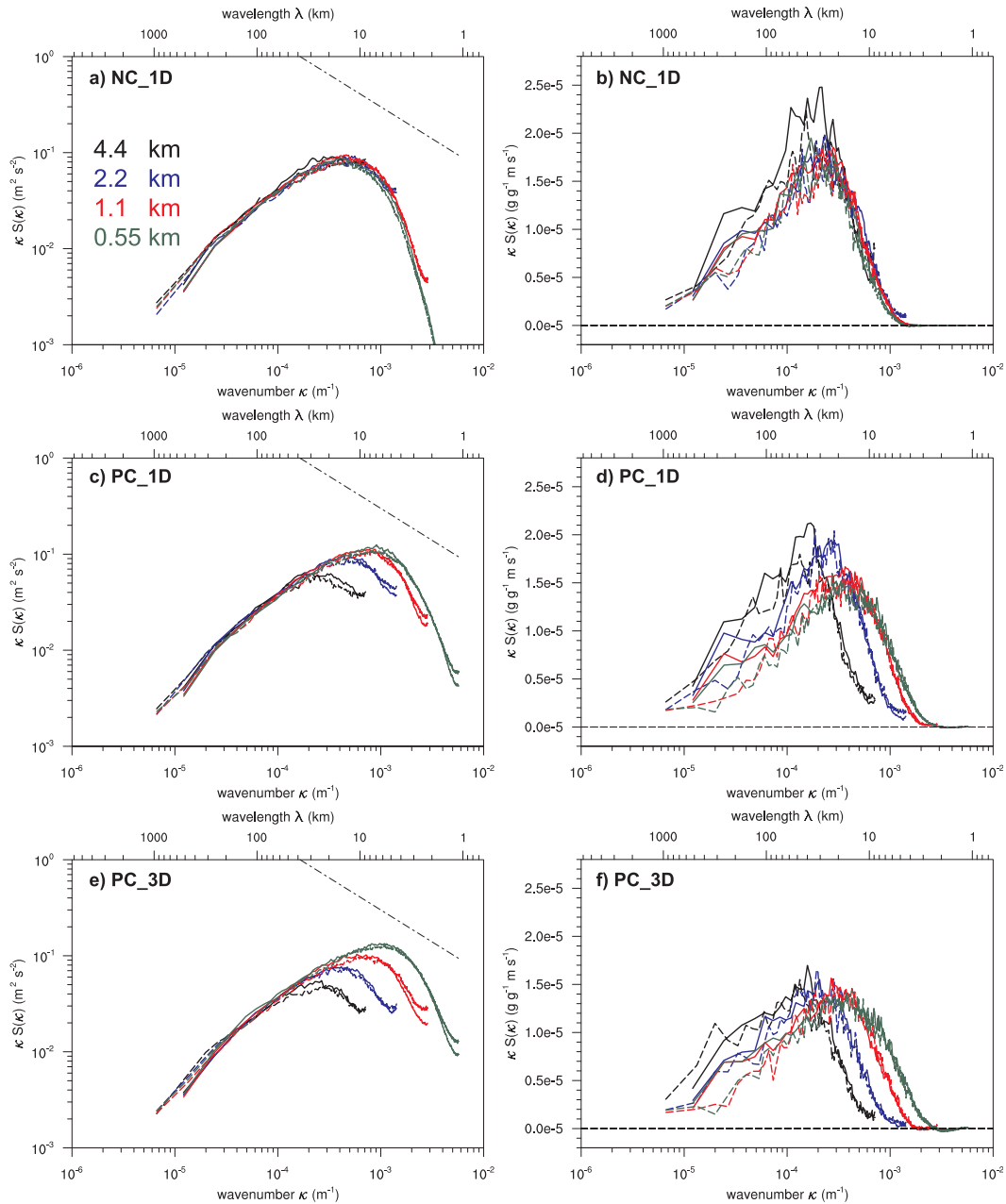


FIG. 15. Spectra of (a),(c),(e) vertical velocity and (b),(d),(f) cospectra of vertical velocity and water vapor mixing ratio at 6 km MSL and averaged at 1600 UTC for (top) NC_1D, (middle) PC_1D, and (bottom) PC_3D. One-dimensional Fourier analysis has been performed for the Alpine region in north–south (solid) and east–west (dashed) direction and (co)spectral densities have been averaged subsequently. The linear ordinate in (b),(d), and (f) has been chosen such that the integrals correspond to the resolved turbulent water vapor flux $\langle q'_w w' \rangle$ [see Eq. (15)].

5. Discussion

The results demonstrate numerical convergence of bulk flow properties for the considered episode of moist orographic convection. NC_1D revealed that numerical

convergence is evident in bulk flow properties of complex real-case simulations, as intuitively expected from a consistent and stable numerical model (Lax and Richtmyer 1956). In analogy to the numerical convergence of large-eddy simulations of the convective

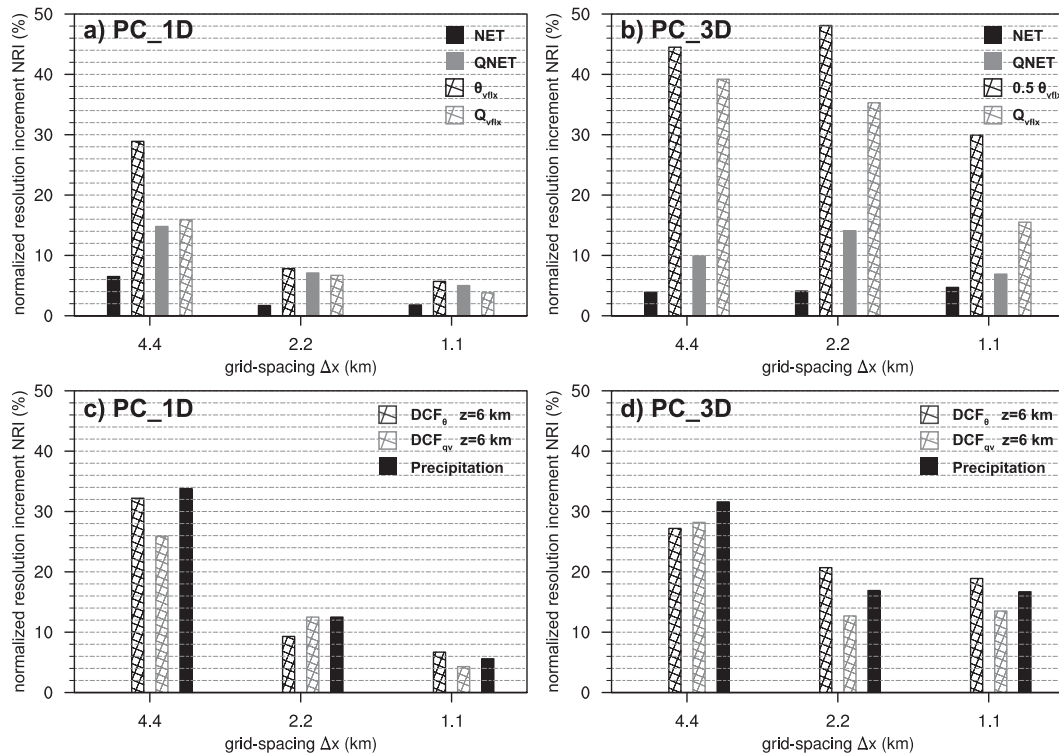


FIG. 16. Normalized resolution increments NRI (%) for (a),(b) volume-integrated heat/moisture tendencies and (c),(d) deep convective fluxes DCF and surface precipitation for (left) PC_1D and (right) PC_3D. The full definition of NRI is provided in Eq. (17). Note that NRI for θ_{vflx} has been scaled by 0.5 in (b).

boundary layer (see Mason and Brown 1999), kilometer-scale cloud-resolving simulations of bulk properties are related to deep convection converge.

The detected monotonic decrease of model errors in NC_1D toward the 0.55-km run exemplifies a systematic numerical convergence of real-case cloud-resolving simulations. The exact order of convergence appears to be of secondary importance, as it might be affected by parameterization schemes and chaotic components in the modeling system. Although we designed our experiments carefully such that boundary and initial conditions as well as the applied turbulence parameterization are grid independent, the convergence might in principle be modulated by physical parameterizations that may react differently to the modified resolved dynamics (Boer and Denis 1997). However, this complication appears unable to disrupt convergence, at least for the modeling system under consideration.

It is also of interest to briefly address the “consistency” of the model. This term is here understood in its usual meaning in numerical analysis: that is, a scheme is said to be consistent if its truncation error per time step tends to zero with Δx , Δy , $\Delta z \rightarrow 0$ and $\Delta t \rightarrow 0$. It is important to note that we are unable to strictly prove consistency—despite the demonstration of numerical

convergence. This inability may be surprising at first glance, as numerical convergence and consistency are closely related through the Lax–Richtmyer theorem (Lax and Richtmyer 1956). However, despite this equivalence, we cannot draw a strict conclusion about consistency, as our statement of numerical convergence merely guarantees convergence, not necessarily convergence toward the correct solution. The assessment of consistency thus requires another approach, and it is indeed questionable whether consistency can be proven for a full atmospheric model such as the one considered. It is likely that one can convince oneself that the dynamical core of an atmospheric model is consistent, for instance using careful numerical analysis and a combination of idealized tests (as the one treated in Fig. 1) and analytical solutions. Yet it is questionable whether this approach can strictly be followed when including a full parameterization package.

The results obtained within the physical convergence framework (PC_1D and PC_3D) impart further credibility and usefulness to explicit modeling of moist convection at kilometer scales. Of particular interest is that the simulated net tendencies are mostly insensitive to the grid spacing, although the energy-containing scales at the high frequency end of the resolved spectrum were

found to depend on the grid spacing (see Figs. 6 and 15). In contrast to previous studies of convective systems over flat terrain, the alpine topography could potentially provide a large-scale forcing that supports convergence of simulations of orographic convection. The diurnal cycle of the lateral fluxes into the control volume (e.g., Figs. 8a,c) may be interpreted as a manifestation of this large-scale forcing, although this forcing itself is generated within the computational domain.

With respect to accuracy, the spread obtained between different resolutions in PC_1D or PC_3D might be considered subjectively as either sufficiently converged or as inadequately large. Compared to uncertainties that might arise from specific model components, the sensitivity of the bulk model behavior to the grid spacing appears, however, to be small. The influence of the grid spacing and the subgrid mixing on the bulk alpine-scale flow appears to be small, for instance in comparison to a significant impact of explicit numerical diffusion on the alpine-scale dynamics (Langhans et al. 2012b). Compared to the previous simulations, a significantly smoother topography and a different model setup (see section 3) have been applied in the current study. The overall effect of these differences appears to reduce the energy available at the grid scale and thereby to limit the upscaling of energy seen in our previous study.

The large sensitivity of the total vertical transport found in PC_3D requires further discussion, although the related net heating and moistening rates were found to be hardly sensitive to resolution. The explicit dependency of the subgrid-scale vertical transport to the horizontal grid spacing (see Figs. 13f,h) strongly affects the total vertical fluxes and prevents a decreasing resolution sensitivity with smaller grid spacings—that is, physical convergence—for some bulk properties (see Fig. 16b).

However, it is questionable whether the assumption of isotropic turbulence [one characteristic turbulent length scale for both horizontal and vertical turbulent mixing; see Eq. (13)] is applicable to kilometer scales. Atmospheric scales may indeed reveal considerable spatial anisotropy at scales outside the inertial subrange (Pedlosky 1987, chapter 4.2). It is speculated that directional eddy viscosities might improve the physical convergence in PC_3D.

6. Summary and conclusions

This paper has addressed numerical and physical bulk convergence properties of moist convection as simulated with horizontal grid spacings of 4.4, 2.2, 1.1, and 0.55 km. Compared to previous studies that considered the convergence of the structure and evolution of single convective cloud systems, we focused on the convergence

of bulk quantities in an ensemble of convective cells over the Alps. To this end, real-case simulations with resolution-independent topography have been conducted over nine consecutive days in July 2006, each day characterized by locally triggered deep convection over complex topography. Our analysis has focused on averages over the 9-day period.

The bulk properties under investigation were the alpine-scale heat and moisture budgets in a large control volume with its top at 4 km, the bulk vertical exchange through the volume's top, the bulk deep convective fluxes at 6 km MSL, and the area-averaged surface precipitation. The transport at 4 km MSL has been regarded as an estimate for the exchange between the planetary boundary layer and the free atmosphere.

Numerical convergence of bulk properties was studied using a fixed turbulent length scale, such that different resolutions are applied to flows with constant Reynolds number. The emerging energetic scales were indeed found to be independent of numerical resolution. For the model and simulation period considered, results show that all bulk properties converge systematically toward the 0.55-km solution. The simulations converge at a surprisingly coarse resolution and the mean diurnal cycles of bulk heating/moistening and vertical fluxes are nearly resolution independent in the range of grid spacings considered.

Physical convergence of bulk properties was explored for simulations characterized by Reynolds numbers that increase with computational resolution. To address the uncertainty related to the parameterization of subgrid turbulent mixing at kilometer scales, results were presented for both a 1D mesoscale and a 3D LES closure. For the 1D approach, our results illustrate the physical convergence of all considered bulk properties; that is, the resolution sensitivity is found to decrease systematically with smaller grid spacings. Moreover, the influence of resolution is generally small for the 1D approach. A less obvious physical convergence behavior was found for the 3D LES approach since some of the investigated bulk properties revealed a less systematic reduction of the resolution sensitivity with smaller grid spacings.

Nevertheless, even for the 3D LES approach, the influence of numerical resolution on the net heating/moistening rates and on surface precipitation was found to be very small, despite an intensification of small-scale dynamics with higher resolution. The weak sensitivity in the simulations using a 3D LES closure is explained by an increased latent heat release that balances the decreased turbulent heat entrainment with higher resolution. This compensation effect can qualitatively be understood, but the high degree of compensation is nevertheless surprising.

The simulations converge even in terms of more complex quantities. For both turbulence closures the influence of the numerical resolution on surface precipitation decreases continuously with higher resolution. For instance, a difference of $\sim 30\%$ between the mean diurnal cycles of precipitation at 4.4 and 2.2 km decreases to a difference of merely 5% and 16% between 1.1 and 0.55 km for the 1D-mesoscale and the 3D LES turbulence closure, respectively. These findings are particularly encouraging as the grid spacing required to simulate the area-averaged precipitation appears not to be controlled by eddy-resolving scales or by the subgrid-scale mixing parameterization.

In short, although a 0.55-km grid spacing is insufficient to resolve small-scale dynamical processes such as turbulent entrainment, convection-permitting resolutions seem to be sufficient to obtain physical convergence of bulk properties in real-case simulations. The less systematic physical convergence found for some bulk properties in simulations using a 3D LES closure did not involve an increased resolution sensitivity of the net heating/moistening and of surface precipitation.

From a practical point of view, our results contribute to an enhanced credibility of kilometer-scale simulations and strengthen the physical validity of the approach. The main limitation of the study relates to the consideration of one single synoptic episode dominated by thermally driven orographic convection. More specifically, further analysis is required to understand the influence of the large-scale topographic forcing on the bulk convergence. Additional studies will be needed to address the convergence issue also for other atmospheric conditions and for different synoptic situations such as cases with frontal convection.

Acknowledgments. This work has been funded by and established in the framework of the Center for Climate Systems Modeling (C2SM) at ETH Zurich. We thank MeteoSwiss (particularly Oliver Fuhrer) for a constructive collaboration on model development and set up and Daniel Lüthi for his technical support; constructive comments have been provided by three anonymous reviewers. The Swiss National Supercomputing Centre (CSCS) is acknowledged for providing access to its high-performance compute clusters; access to the COSMO model was kindly provided by the COSMO consortium.

APPENDIX

Linear Hydrostatic Gravity Wave Simulations

The numerical setup used for the COSMO simulations of a hydrostatic gravity wave is generally identical

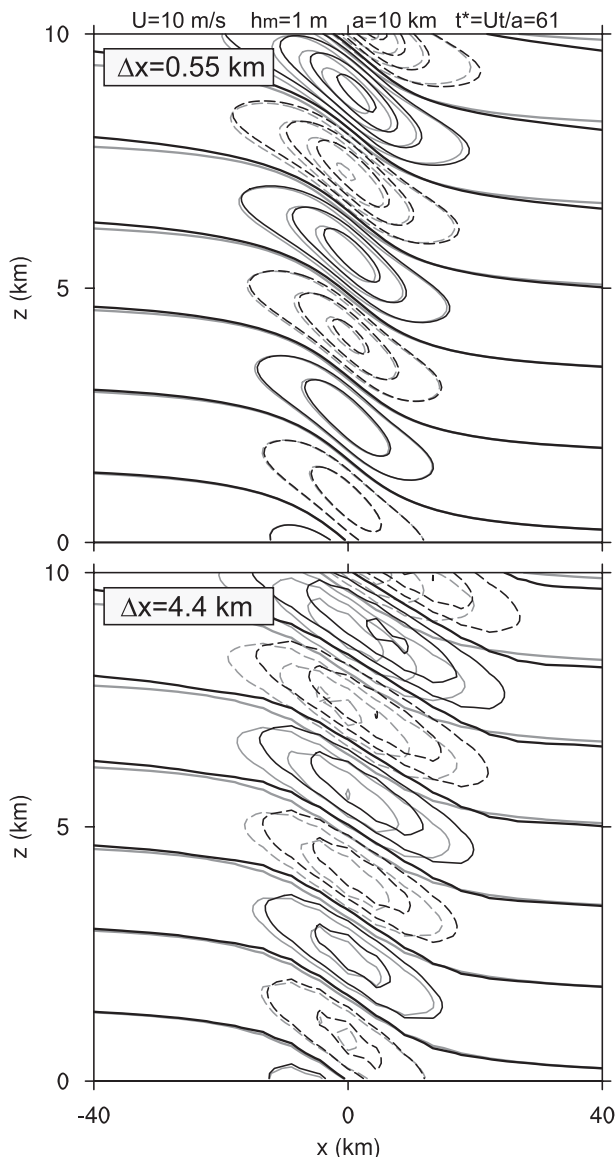


FIG. A1. Vertical velocity after 17 h ($\bar{U}t/a \approx 61$) from simulations of a linear hydrostatic mountain wave for flow over a 1-m-high and 10-km-wide mountain using (top) $\Delta x = 0.55$ km and (bottom) $\Delta x = 4.4$ km. Black and gray contour lines show vertical velocity for the simulation and the linear solution (computed at model grid points), respectively. Contour interval is 0.4 m s^{-1} and the amplitude is scaled to a 1000-m-high mountain.

to the real-case simulations. Horizontal grid spacings of 17.6, 8.8, 4.4, 2.2, 1.1, and 0.55 km and corresponding time steps of 120, 60, 30, 15, 8, and 4 s are used to simulate the inviscid flow. In contrast to the stretched grid applied in the real-case runs, a constant vertical grid spacing $\Delta z = 100$ m has been chosen. The domain is about 500 km long and 20 km deep with a bell-shaped mountain of half-width $a = 10$ km and height $h_m = 1$ m.

Radiative lateral and free-slip surface boundary conditions are used, and a 9-km deep Rayleigh-sponge absorbs energy at the top. Following Durran and Klemp (1982a), for example, an isothermal thermodynamic profile ($\bar{T} = 250$ K) has been chosen since for this profile the analytical solution of the linearized equations is known. The background wind speed is $\bar{U} = 10$ m s⁻¹. Vertical velocity patterns are analyzed at $t^* = \bar{U}t/a \approx 60$, but almost identical results have been found at $t^* = \bar{U}t/a \approx 120$. The L2 norm (RMSE) shown in Fig. 1 has been computed for grid points below 7.5 km and within 40 km of the center of the mountain.

Figure A1 shows the analytical solution for vertical velocity and simulation results for grid spacings Δx of 550 m and 4.4 km. The comparison against the analytical solution reveals an error reduction with higher resolution, that is, numerical convergence.

REFERENCES

- Baldauf, M., A. Seifert, J. Förstner, D. Majewski, M. Raschendorfer, and T. Reinhardt, 2011: Operational convective-scale numerical weather prediction with the COSMO model: Description and sensitivities. *Mon. Wea. Rev.*, **139**, 3887–3905.
- Blackadar, A. K., 1962: The vertical distribution of wind and turbulent exchange in a neutral atmosphere. *J. Geophys. Res.*, **67**, 3095–3102.
- Boer, G. J., and B. Denis, 1997: Numerical convergence of the dynamics of a GCM. *Climate Dyn.*, **13**, 359–374.
- Bott, A., 1989: A positive definite advection scheme obtained by nonlinear renormalization of the advective fluxes. *Mon. Wea. Rev.*, **117**, 1006–1015.
- Bryan, G. H., J. C. Wyngaard, and J. M. Fritsch, 2003: Resolution requirements for simulations of deep moist convection. *Mon. Wea. Rev.*, **131**, 2394–2416.
- Cheng, A., and K.-M. Xu, 2006: Simulation of shallow cumuli and their transition to deep convective clouds by cloud-resolving models with different third-order turbulence closures. *Quart. J. Roy. Meteor. Soc.*, **132**, 359–382.
- Craig, G. C., and A. Dörnbrack, 2008: Entrainment in cumulus clouds: What resolution is cloud-resolving? *J. Atmos. Sci.*, **65**, 3978–3988.
- Cullen, M. J. P., and A. R. Brown, 2009: Large eddy simulation of the atmosphere on various scales. *Philos. Trans. Roy. Soc. London*, **367**, 2947–2956.
- Doms, G., and J. Förstner, 2004: Development of a kilometer-scale NWP-system: LMK. *COSMO Newsletter*, No. 4, 159–167. [Available online at <http://www.cosmo-model.org/content/model/documentation/newsLetters/default.htm>.]
- Durran, D. R., and J. B. Klemp, 1982a: The effects of moisture on trapped mountain lee waves. *J. Atmos. Sci.*, **39**, 2490–2506.
- , and —, 1982b: On the effects of moisture on the Brunt-Väisälä frequency. *J. Atmos. Sci.*, **39**, 2152–2158.
- Fiori, E., A. Parodi, and F. Siccardi, 2010: Turbulence closure parameterization and grid spacing effects in simulated supercell storms. *J. Atmos. Sci.*, **67**, 3870–3890.
- Fuhrer, O., and C. Schär, 2005: Embedded cellular convection in moist flow past topography. *J. Atmos. Sci.*, **62**, 2810–2828.
- Grabowski, W. W., 2001: Coupling cloud processes with the large-scale dynamics using the Cloud-Resolving Convection Parameterization (CRCP). *J. Atmos. Sci.*, **58**, 978–997.
- Grell, G. A., L. Schade, R. Knoche, A. Pfeiffer, and J. Egger, 2000: Nonhydrostatic climate simulations of precipitation over complex terrain. *J. Geophys. Res.*, **105**, 29 595–29 608.
- Heise, E., M. Lange, B. Ritter, and R. Schrodin, 2003: Improvement and validation of the multi-layer soil model. *COSMO Newsletter*, No. 3, 198–203. [Available online at <http://www.cosmo-model.org/content/model/documentation/newsLetters/default.htm>.]
- Hohenegger, C., P. Brockhaus, and C. Schär, 2008a: Towards climate simulations at cloud-resolving scales. *Meteor. Z.*, **17**, 383–394.
- , A. Walser, W. Langhans, and C. Schär, 2008b: Cloud-resolving ensemble simulations of the August 2005 Alpine flood. *Quart. J. Roy. Meteor. Soc.*, **134**, 889–904.
- Jäger, E. B., I. Anders, D. Lüthi, B. Rockel, C. Schär, and S. I. Seneviratne, 2008: Analysis of ERA40-driven CLM simulations for Europe. *Meteor. Z.*, **17**, 349–367.
- Khairoutdinov, M. F., and D. A. Randall, 2001: A cloud resolving model as a cloud parameterization in the NCAR Community Climate System Model: Preliminary results. *Geophys. Res. Lett.*, **28**, 3617–3620.
- , S. K. Krueger, C.-H. Moeng, P. A. Bogenschutz, and D. A. Randall, 2009: Large-eddy simulation of maritime deep tropical convection. *J. Adv. Model. Earth Syst.*, **1**, 15, doi:10.3894/JAMES.2009.1.15.
- Klemp, J., and R. Wilhelmson, 1978: Simulation of three-dimensional convective storm dynamics. *J. Atmos. Sci.*, **35**, 1070–1096.
- Langhans, W., O. Fuhrer, and J. Schmidli, 2012a: Description and application of a budget-diagnosis tool in COSMO. *COSMO Newsletter*, No. 12, 43–51. [Available online at <http://www.cosmo-model.org/content/model/documentation/newsLetters/default.htm>.]
- , J. Schmidli, and C. Schär, 2012b: Mesoscale impacts of explicit numerical diffusion in a convection-permitting model. *Mon. Wea. Rev.*, **140**, 226–244.
- Lax, P. D., and R. D. Richtmyer, 1956: Survey of the stability of linear finite difference equations. *Commun. Pure Appl. Math.*, **9**, 267–293.
- Lean, H. W., P. A. Clark, M. Dixon, N. M. Roberts, A. Fitch, R. Forbes, and C. Halliwell, 2008: Characteristics of high-resolution versions of the Met Office Unified Model for forecasting convection over the United Kingdom. *Mon. Wea. Rev.*, **136**, 3408–3424.
- Lilly, D. K., 1962: On the numerical simulations of buoyant convection. *Tellus*, **14**, 148–172.
- Lugauer, M., and P. Winkler, 2005: Thermal circulation in South Bavaria—Climatology and synoptic aspects. *Meteor. Z.*, **14**, 15–30.
- Mason, P. J., 1994: Large-eddy simulation: A critical review of the technique. *Quart. J. Roy. Meteor. Soc.*, **120**, 1–26.
- , and R. I. Sykes, 1982: A two-dimensional numerical study of horizontal roll vortices in an inversion capped planetary boundary layer. *Quart. J. Roy. Meteor. Soc.*, **108**, 801–823.
- , and N. S. Callen, 1986: On the magnitude of the subgrid-scale eddy coefficient in large-eddy simulations of turbulent channel flow. *J. Fluid Mech.*, **162**, 439–462.
- , and A. R. Brown, 1999: On subgrid models and filter operations in large eddy simulations. *J. Atmos. Sci.*, **56**, 2101–2114.
- Mellor, G. L., and T. Yamada, 1982: Development of a turbulence closure model for geophysical fluid problems. *Rev. Geophys. Space Phys.*, **20**, 851–875.

- MeteoSchweiz, cited 2006: Juli 2006: Klimatologisch ein extremer Monat. [Available online at http://www.meteoschweiz.admin.ch/web/de/wetter/wetterereignisse/juli_2006_erste_bilanz.html.]
- Moeng, C.-H., P. P. Sullivan, M. F. Khairoutdinov, and D. A. Randall, 2010: A mixed scheme for subgrid-scale fluxes in cloud-resolving models. *J. Atmos. Sci.*, **67**, 3692–3705.
- Pedlosky, J., 1987: *Geophysical Fluid Dynamics*. Springer, 710 pp.
- Petch, J. C., A. R. Brown, and M. E. B. Gray, 2002: The impact of horizontal resolution on the simulations of convective development over land. *Quart. J. Roy. Meteor. Soc.*, **128**, 2031–2044.
- Pope, S. B., 2000: *Turbulent Flows*. Cambridge University Press, 770 pp.
- Raschendorfer, M., 2001: The new turbulence parameterization of LM. *COSMO Newsletter*, No. 1, 90–98. [Available online at <http://www.cosmo-model.org/content/model/documentation/newsLetters/default.htm>.]
- Raymond, W. H., 1988: High-order low-pass implicit tangent filters for use in finite area calculations. *Mon. Wea. Rev.*, **116**, 2132–2141.
- Reinhardt, T., and A. Seifert, 2006: A three-category ice-scheme for LMK. *COSMO Newsletter*, No. 6, 115–120. [Available online at <http://www.cosmo-model.org/content/model/documentation/newsLetters/default.htm>.]
- Richard, E., A. Buzzi, and G. Zängl, 2007: Quantitative precipitation forecasting in the Alps: The advances achieved by the Mesoscale Alpine Programme. *Quart. J. Roy. Meteor. Soc.*, **133**, 831–846.
- Ritter, B., and J. F. Geleyn, 1992: A comprehensive radiation scheme for numerical weather prediction models with potential applications in climate simulations. *Mon. Wea. Rev.*, **120**, 303–325.
- Rosinger, E. E., 1980: Stability and convergence for non-linear difference schemes are equivalent. *IMA J. Appl. Math.*, **26**, 143–149.
- Schlemmer, L., C. Hohenegger, J. Schmidli, C. S. Bretherton, and C. Schär, 2011: An idealized cloud-resolving framework for the study of midlatitude diurnal convection over land. *Mon. Wea. Rev.*, **68**, 1041–1057.
- Schmidli, J., and R. Rotunno, 2010: Mechanisms of along-valley winds and heat exchange over mountainous terrain. *J. Atmos. Sci.*, **67**, 3033–3047.
- Schwartz, C. S., and Coauthors, 2009: Next-day convection-allowing WRF model guidance: A second look at 2-km versus 4-km grid spacing. *Mon. Wea. Rev.*, **137**, 3351–3372.
- Skamarock, W. C., 2004: Evaluating mesoscale NWP models using kinetic energy spectra. *Mon. Wea. Rev.*, **132**, 3019–3032.
- Smagorinsky, J., 1963: General circulation experiments with the primitive equations. *Mon. Wea. Rev.*, **91**, 99–164.
- Steppeler, J., G. Doms, U. Schättler, H. W. Bitzer, A. Gassmann, U. Damrath, and G. Gregoric, 2003: Meso-gamma scale forecasts using the nonhydrostatic model LM. *Meteor. Atmos. Phys.*, **82**, 75–96.
- Stull, R. B., 1988: *An Introduction to Boundary Layer Meteorology*. Kluwer Academic, 666 pp.
- Takemi, T., and R. Rotunno, 2003: The effects of subgrid model mixing and numerical filtering in simulations of mesoscale cloud systems. *Mon. Wea. Rev.*, **131**, 2085–2101; Corrigendum, **133**, 339–341.
- Weinbrecht, S., and P. J. Mason, 2008: Stochastic backscatter for cloud-resolving models. Part I: Implementation and testing in a dry convective boundary layer. *J. Atmos. Sci.*, **65**, 123–139.
- Weisman, M. L., W. C. Skamarock, and J. B. Klemp, 1997: The resolution dependence of explicitly modeled convective systems. *Mon. Wea. Rev.*, **125**, 527–548.
- Weissmann, M., F. J. Braun, L. Ganter, G. J. Mayr, S. Rahm, and O. Reitebuch, 2005: The Alpine mountain–plain circulation: Airborne Doppler lidar measurements and numerical simulations. *Mon. Wea. Rev.*, **133**, 3095–3109.
- Weusthoff, T., F. Ament, M. Arpagaus, and M. W. Rotach, 2010: Assessing the benefits of convection-permitting models by neighborhood verification: Examples from MAP D-PHASE. *Mon. Wea. Rev.*, **138**, 3418–3433.
- Wicker, L. J., and W. C. Skamarock, 2002: Time-splitting methods for elastic models using forward time schemes. *Mon. Wea. Rev.*, **130**, 2088–2097.
- Wyngaard, J. C., 2004: Toward numerical modeling in the “Terra Incognita.” *J. Atmos. Sci.*, **61**, 1816–1826.